2008

Modeling of high speed water jets in air

Anirban Guha
University of Windsor

MODELING OF HIGH SPEED WATER JETS IN AIR

by

ANIRBAN GUHA

A Thesis

Submitted to the Faculty of Graduate Studies through

Mechanical, Automotive and Materials Engineering

in Partial Fulfillment of the Requirements for

the Degree of Master of Applied Science at the

University of Windsor

Windsor, Ontario, Canada

2008

Canada

Author's Declaration of Originality

I hereby certify that I am the sole author of this thesis and that no part of this thesis has been published or submitted for publication.

I certify that, to the best of my knowledge, my thesis does not infringe upon anyone's copyright nor violate any proprietary rights and that any ideas, techniques, quotations, or any other material from the work of other people included in my thesis, published or otherwise, are fully acknowledged in accordance with the standard referencing practices. Furthermore, to the extent that I have included copyrighted material that surpasses the bounds of fair dealing within the meaning of the Canada Copyright Act, I certify that I have obtained a written permission from the copyright owner(s) to include such material(s) in my thesis and have included copies of such copyright clearances to my appendix.

I declare that this is a true copy of my thesis, including any final revisions, as approved by my thesis committee and the Graduate Studies office, and that this thesis has not been submitted for a higher degree to any other University of Institution.

ABSTRACT

High speed water jets in air are typically used in industrial cleaning operations. Vigorous interaction between the jet and the surrounding air brings about an exchange of mass and momentum which results in the spreading of the jet. An experimental investigation of pressure distribution on a target plate placed in the jet flow field has been performed and analyzed. The main purpose of this research is to numerically simulate the flow characteristics of high speed water jets in air. Since, to the best of our knowledge, there is no numerical model to describe the flow physics of high speed jets, novel numerical models are proposed. Results obtained from the numerical simulation are compared to the existing experimental results in the literature, as well as our own experimental data. Different flow properties were analyzed to provide considerable insight into the physics of these flows.

Dedicated to

My Country, India

and

My Mother

ACKNOWLEDGEMENTS

Firstly, I would like to express my thanks to the Almighty and to my Mother, Mallika. I would like to express my deep and sincere gratitude to my supervisors, Dr. R. M. Barron and Dr. R. Balachandar for not only giving me this opportunity but also for their generous help, unceasing advice and patience during the course of this study. I would also like to thank my fiancé Tanaya and my best friend Subhranil for their support and inspiration.

I would like to express my sincere thanks to my thesis committee members, Dr G. W. Rankin, Dr. T. Bolisetti and Mr. D. Baulier. I would also like to thank Valiant Machine and Tool Inc. for providing financial support as well as experimental facilities. Sincere thanks to SHARCNET for providing our research group with high performance computing resource.

Finally, I would like to thank my colleagues, Arindam, Atefeh, Feng, Zheng Zhang and Arjun for supporting me at all times. Also I would like to express my sincere thanks to Dr. P. Diamessis of Civil and Environmental Engineering Department, Cornell University, for not only inviting me to his University and encouraging my research work but also for instilling numerous academic as well as moral values in me.

TABLE OF CONTENTS

CHAPTER

LIST OF TABLES

LIST OF FIGURES

NOMENCLATURE

b	Half-width of the jet based on velocity
b_w	Half-width of the jet based on volume flow rate of water
C	Spread coefficient of the outer region of the jet
C_D	Drag coefficient
D	Diameter of the nozzle
$G_{k,m}$	Production of turbulent kinetic energy
k	Turbulent kinetic energy
k_1	Spread coefficient of the inner region of the jet
K_{ij}	Interphase momentum exchange coefficient
m	Linear decay slope of target pressure along the centreline of the jet
$\dot{M}$	Mass flux of water phase
$\dot{M}_0$	Mass flux of water phase at nozzle exit
$\dot{m}_{i \to j}$	Mass transfer from phase-i to phase-j
Oh	Ohnesorge Number
P	Pressure at the target plate
P_{atm}	Atmospheric pressure
P_{inlet}	Pressure at the nozzle inlet
P_{inlet}^{total}	Total pressure at nozzle inlet
P_{exit}^{total}	Total pressure at nozzle exit
q	Volume flow rate of water at any point in the jet
q_m	Volume flow rate of water at the centreline of the jet

r	Radial distance
R	Radial width of the droplet zone of a jet
R_{inner}	Radial width of the inner region of the jet
R_{outer}	Radial width of the outer region of the jet
R_{Patm}	Radial distance where $P=P_{atm}$
Re	Reynolds Number
Re_{rel}	Relative Reynolds Number
s	Surface tension between water and air
U_{target}	Mean velocity at the target
V	Velocity
V_0	Water phase velocity at nozzle exit
We	Weber Number
x	Axial distance
x_b	Break-up length of the jet
α_0	Volume fraction of water at nozzle exit
α	Volume fraction
ε	Turbulent dissipation rate
μ	Viscosity
$\mu_{t,m}$	Turbulent viscosity
ρ	Density
σ	Cavitation Number

Subscripts:

a	Air
a	Case (a)
b	Case (b)
g	Gas
i	Phase index
inlet	Nozzle Inlet
l	Liquid
w	Water

Chapter 1

INTRODUCTION

1.1   Introduction

High speed turbulent water jets are extensively used in industrial cleaning and cutting applications. The velocity of these jets varies from ~ 80-300 m/s depending upon the application. These jets may interact vigorously with the surrounding atmosphere and diffuse very much like submerged jets (Rajaratnam et al., 1994). They exhibit a high velocity coherent core surrounded by an annular cloud of water droplets moving in an entrained air stream.

Leu et al. (1998) discussed the anatomy of high speed water jets in air. Much like Rajaratnam et al. (1994, 1998), they divided the jet into three distinct regions:

a)   Initial Region: In the region close to the nozzle exit, instabilities cause eddies which brings about transfer of mass and momentum between air and water and this process of air entrainment breaks up continuous water into droplets. There remains a wedge shaped potential core surrounded by a mixing layer in which the velocity is equal to the nozzle exit velocity.

b)   Main Region: The effect of air dynamics and continuous interaction of water with surrounding air results in the break up of the water jet stream into droplets. There is a very high degree of air entrainment and the size of water droplets decreases with the increase in radial distance from the axis. Due to momentum transfer to the surrounding air, the mean velocity of the water jet decreases and the jet expands. Between the water

droplet zone and the surrounding air, there is a mist region in which the drops are very small and the velocity is negligible.

c)   Final Region: This diffusion zone is produced by the complete disintegration of the jet into very small droplets.

Figure 1.1 shows the anatomy of high speed water jets in air.
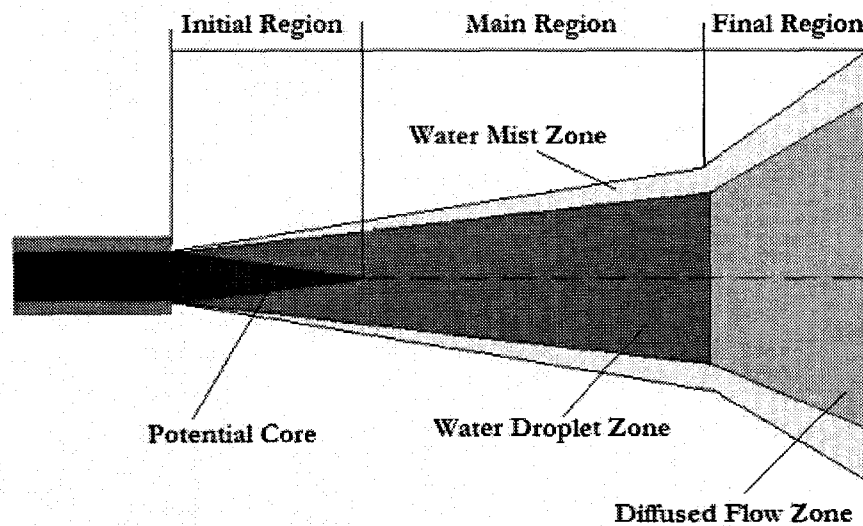
Figure 1.1: Anatomy of High Speed Water Jet in Air [Leu et al. (1998)]

1.2   Previous Works

The physics of high speed water jets in air has numerous interesting aspects and presents a challenging area for research. Rajaratnam et al. (1998) experimentally observed that the volume fraction of water along the centreline of the jet falls drastically, although there is almost no loss in the centreline velocity for around 100 nozzle diameters downstream. Leach et al. (1966) experimentally obtained the pressure distribution on a target plate placed in the jet flow field. They concluded that the normalized pressure

distribution is similar for jets emanating from different nozzles as well as at different operating pressures.

1.3 Scope for Future Work

Although high speed water jets in air have significant industrial application, there has been limited research work published in this field. Moreover, to the best of our knowledge, numerical modeling of high speed water jets in air and validation with reported experimental results has not been done. Hence, there is an enormous scope for numerical modeling and simulation research in this field. From the application point of view, the most important aspect is the pressure distribution on the cleaning or cutting surface placed in the jet flow field. Although the pressure distribution characteristics have been experimentally studied by Leach et al. (1966) and Yanaida and Ohashi (1978, 1980), their studies do not focus on the potential core and water droplets zones which are industrially more relevant. These two zones have significant momentum to deliver to the cleaning or the cutting surface. Hence, the focus of our study will be on those two regions of the jet.

1.4 Thesis Outline

This thesis briefly covers the previous works reported in this area of study. Since the problems to be considered fall into the category of turbulent multiphase flows, a brief overview on this topic has been provided.

The main focus of the thesis is to build numerical models that can predict the flow physics of high speed turbulent water jets in air with considerable accuracy. Novel numerical models have been proposed in this thesis and incorporated into a commercial CFD package (FLUENT). The results obtained are compared with existing experimental works.

The radial pressure distribution on a target plate placed in a jet flow field has also been measured experimentally and a generalized equation has been formulated. The results obtained from the experiments have been compared with those obtained from the numerical model. Different flow properties have been analyzed to provide considerable insight into the physics of these flows.

Chapter 2

LITERATURE REVIEW

2.1 Introduction

Although the physics of low and moderate speed water jets in air have received significant attention amongst various researchers, similar studies on turbulent high speed water jets (~80-300 m/s) have been limited. Leach et al. (1966) studied the pressure distribution at a target plate placed at a given axial distance from the nozzle. They showed that the pressure distribution along the centreline of a jet is highly dependent on the nozzle geometry. Yanaida and Ohashi (1980) did similar work and formulated a mathematical expression which provides a good fit for axial distances far away from the nozzle exit. Rajaratnam et al. (1994, 1998) studied the velocity and water phase volume fraction distributions in the jet field. Leu et al. (1998) studied the jet anatomy and divided the jet into different zones based on physical characteristics. Lin and Reitz (1998) classified jets according to their break-up regimes and showed that high speed water jets are classified in the atomization regime. Hiroyasu et al. (1991), Arai et al. (1988), Vahedi et al. (2003) and Sou et al. (2007) have shown that jet characteristics can be significantly influenced by nozzle cavitation. Recent experimental and numerical studies of Yoon et al. (2004) on high speed sprays have revealed that the instabilities that produce atomized jets are not yet well understood, while that of moderate and low speed jets are well established. This chapter offers a brief review of the published literature pertinent to the research of turbulent high speed water jets in air.

2.2 Anatomy of Cleaning Jets

Leu et al. (1998) discussed the anatomy of high speed water jets in air and also analytically obtained a relation between the mass flux along the centreline of the jet and the mass flux at the nozzle exit. Much like Rajaratnam et al. (1994, 1998), they divided the jet into three distinct regions:

a) Initial Region: In the region close to the nozzle exit, flow instabilities cause eddies to form, bringing about transfer of mass and momentum between air and water and this process of air entrainment breaks up continuous water into droplets. There remains a wedge-shaped potential core in which the velocity is equal to the nozzle exit velocity, surrounded by a mixing layer.

b) Main Region: The effect of air dynamics and continuous interaction of water with surrounding air results in the break up of the water jet stream into droplets. There is a very high degree of air entrainment and the size of the water droplets decreases with the increase of radial distance from the axis. Due to momentum transfer to the surrounding air, the mean velocity of the water jet decreases and the jet expands. Between the water droplet zone and the surrounding air, there is a mist region in which the drops are very small and the velocity is negligible.

c) Final Region: This diffusion zone is produced by the complete disintegration of the jet into very small droplets. The figure below shows the anatomy of high speed water jets in air.
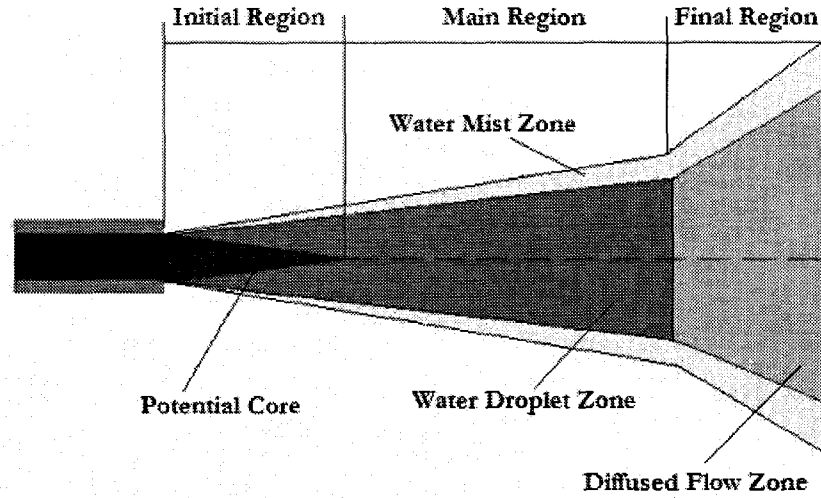
Figure 2.1: Anatomy of High Speed Water Jet in Air [Leu et al. (1998)]

Leu et al. (1998) also determined the dependence of mass flux along the jet centreline

($\dot{M}(x,0)$) on mass flux at the nozzle exit ($\dot{M}_0$). This relationship is as follows:

$$\dot{M}(x,0) = \frac{5.62\dot{M}_0 R_0^{\ 2}}{R^2}$$

(2.1)

where R_0 is the nozzle exit radius and R is the radius of the droplet zone.

2.3 High Speed Water Jets Emanating from Different Nozzles and Their Pressure Characteristics

Leach et al. (1966) studied high speed water jets in air for cutting operations. Their main interest was to see how nozzle geometry and driving pressure can influence the jet characteristics, especially the pressure distribution on a target plate placed in the jet flow

field. Different nozzle geometries were studied as shown in Figure 2.2. The nozzle exit

diameter (D) was 1 mm and the inlet velocity was around 350 m/s.
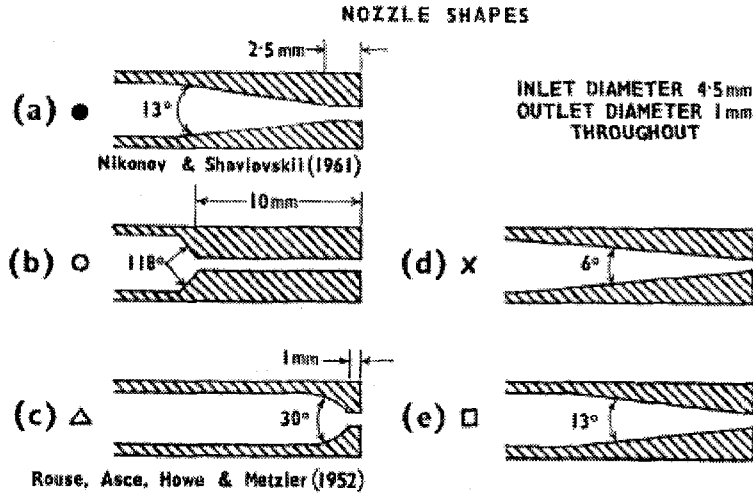
Figure 2.2: Different Nozzle Geometries Used by Leach et al. (1966)

As shown in Figure 2.3, the decay of target pressure along the centreline was least for the

nozzle in Figure 2.2(a), i.e., the converging-straight nozzle. From their study, it was

obvious that nozzle geometry can significantly affect the jet characteristics. Since the best

results were obtained with the converging-straight nozzle, they carried out different

analysis with this type of nozzle. They also studied the pressure distribution in the

direction perpendicular to the jet flow at two different axial distances, $76D$ and $330D$

(Figure 2.4) and analytically obtained the radial pressure distribution using the following

polynomial fit:

$$\frac{P - P_{atm}}{\frac{1}{2}\rho U_{t\,arg\,et}{}^2} = 1 - 3\left(\frac{r}{R_{P_{atm}}}\right)^2 + 2\left(\frac{r}{R_{P_{atm}}}\right)^3 \tag{2.2}$$

where U_{target} is mean velocity at the target and $R_{P_{atm}}$ is the radial distance where $P = P_{atm}$

8
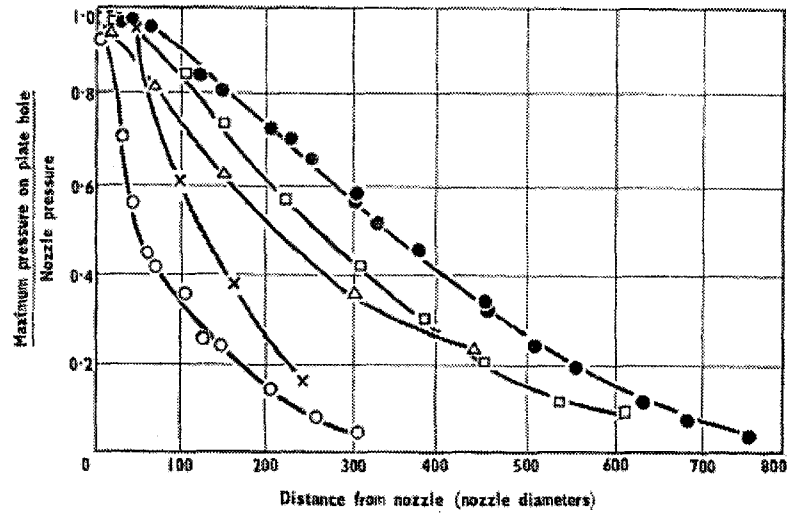
Figure 2.3: Decay of Normalized Pressure along the Centreline for Different Nozzle

Geometries [Leach et al. (1966)]
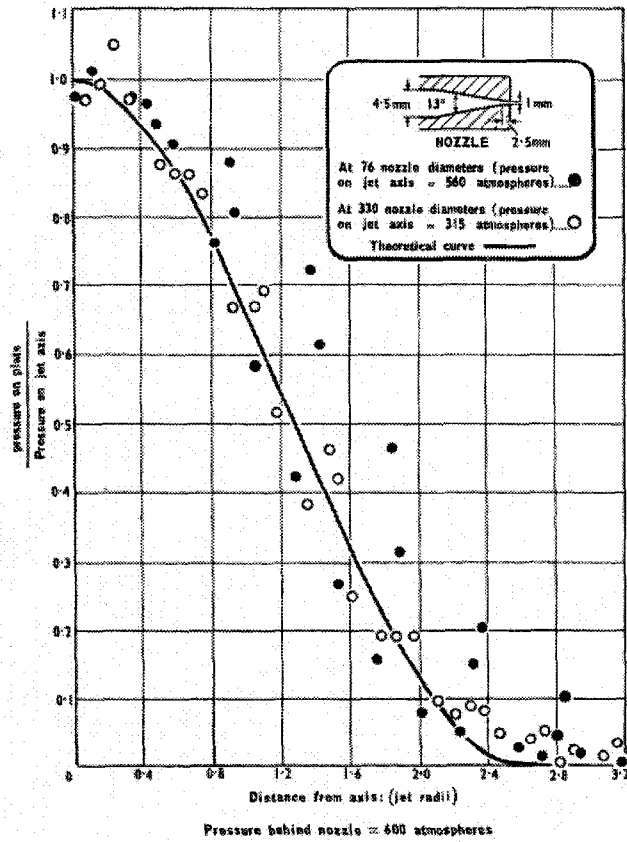
Figure 2.4: Radial Distribution of Normalized Pressure at 76*D* and 330*D* [Leach et

al. (1966)]

From this analysis, Leach et al. found that the normalized static pressure becomes equal to the ambient pressure at around $2.6R_0$, i.e. at around $1.3D$. Outside this region, the shear stress is too small to be able to cut or clean the target surface. They also found that the normalized static pressure distribution collapsed into one curve even when different inlet pressure conditions and different nozzle geometry were used.

Yanaida and Ohashi (1980) analyzed the core and the water droplet zone together and divided the jet flow according to radial distance from the centreline (see Figure 2.5). The inner region is the continuous flow region, the radial width of which varies as

$$R_{inner} = k_1 \sqrt{xR_0}$$ (2.3)

Outside of this region is the droplet flow region, the radial width of which varies as

$$\frac{dR_{outer}}{dx} = \frac{C}{R_0}$$ (2.4)

The constants k_1 and C are Spread Coefficients, related by $C = \dfrac{k_1}{1.9}$. (2.5)
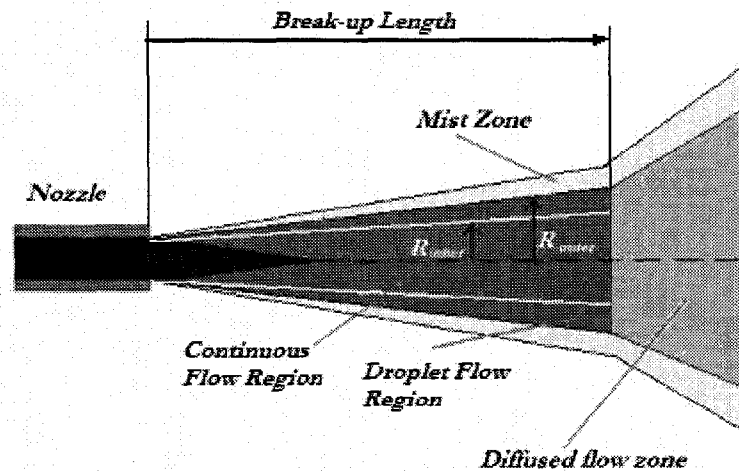
Figure 2.5: Classification of High Speed Water Jets by Radial Distance from

Centreline [Leu et al. (1998)]

They used a set of nozzles to analyze the jets, all of which had a straight portion. They also obtained mathematical relations for the pressure along the centreline. The equation corresponding to the region within the break-up length (x_b) is

$$\frac{P}{P_{inlet}} = 0.00353 + 3.89\left(\frac{1}{k_1^2}\right)\left(\frac{R_0}{x}\right) - 0.00158\left(\frac{k_1^2 \frac{x}{R_0}}{3.89}\right) \qquad (2.6)$$

After the jet break-up, the centreline pressure equation is

$$\frac{P}{P_{inlet}} = 0.00353 + 3.89\left(\frac{1}{k_1^2}\right)\left(\frac{R_0}{x}\right) - 0.00158\left(\frac{0.5C\left(\frac{x-x_b}{R_0}\right)+7}{k_1\sqrt{\frac{x}{R_0}}}\right)^2 \qquad (2.7)$$

The equations were found to match well with their experimental results for $x/D > 350$.
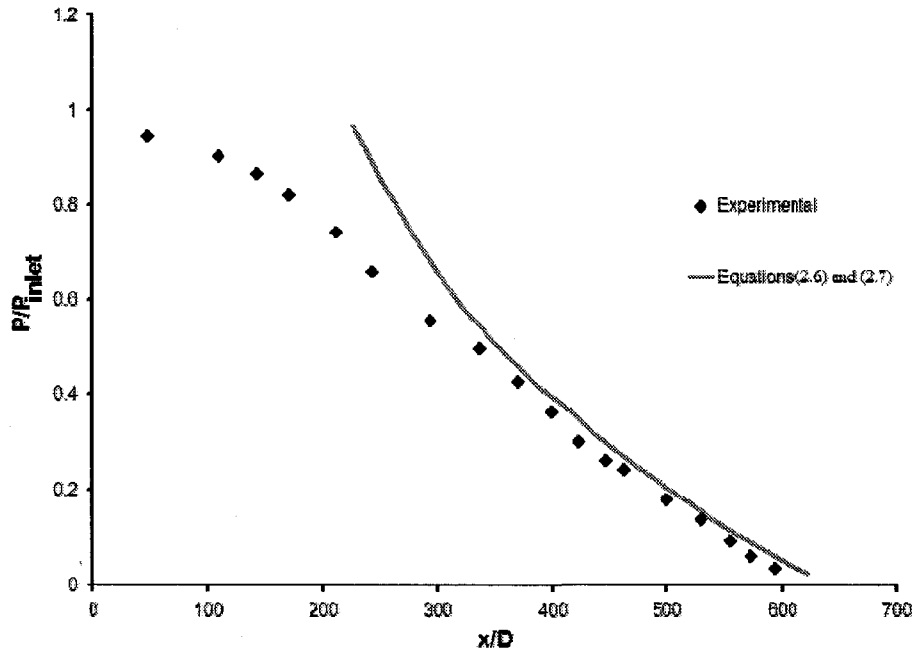
Figure 2.6: Comparison of Experimental Results and Equations (2.6) and (2.7)

[Yanaida et al. (1980)]

11

The figure above is for a converging straight nozzle (D = 1.6mm), P_{inlet} = 14.7 MPa, x_b = 480D, k_1 = 0.12, C = 0.0146.

2.4 Velocity and Volume Fraction Distribution of High Speed Water Jets in Air

Rajaratnam et al. (1994) did experiments mainly with a 2 mm exit diameter nozzle with geometry similar to type-a of Leach et al. (1966) and velocity around 155 m/s. They concluded that these high velocity jets diffuse very much like submerged jet and found that there is a high velocity coherent core surrounded by an annular cloud of water droplets moving in an entrained air stream. They studied the velocity as well as the centreline volume fraction distribution of these high speed jets. Experimentally they found that the centreline velocity remains constant and equal to the nozzle exit velocity for more than 100D and then decays linearly to about 0.25 of nozzle exit velocity at about 2500D (Figure 2.7). Also they found that the radial velocity distribution is similar for x/D greater than 400 (Figure 2.8) and the average radial distance where the jet velocity is 10% of its axial value is 3.9 times the half width (b) based on velocity profile (in case of submerged circular turbulent jets, it is 2.25b). They also inferred that the radius of the central core of the jet increases linearly at a rate of 0.007 while the radius of the surrounding droplet layer increases linearly at a rate of 0.07.
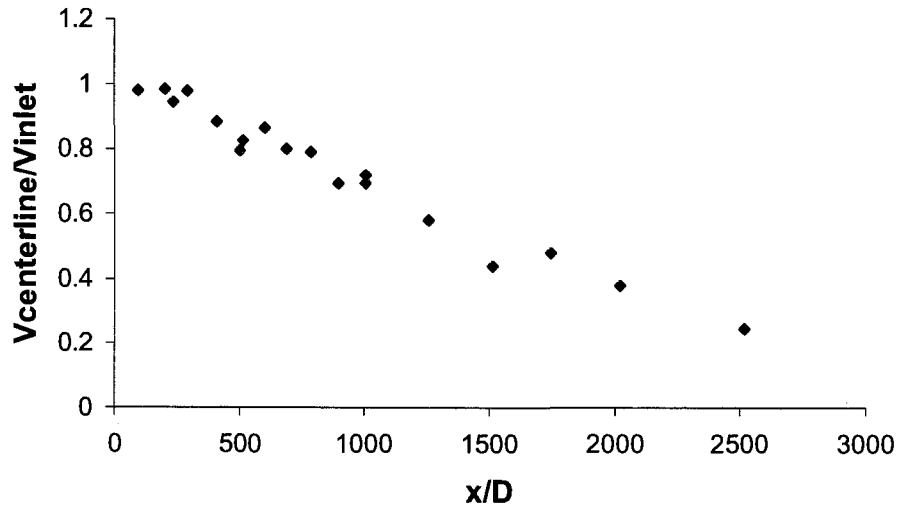
Figure 2.7: Decay of Normalized Centreline Velocity Along the Jet Axis

[Rajaratnam et al. (1994)]
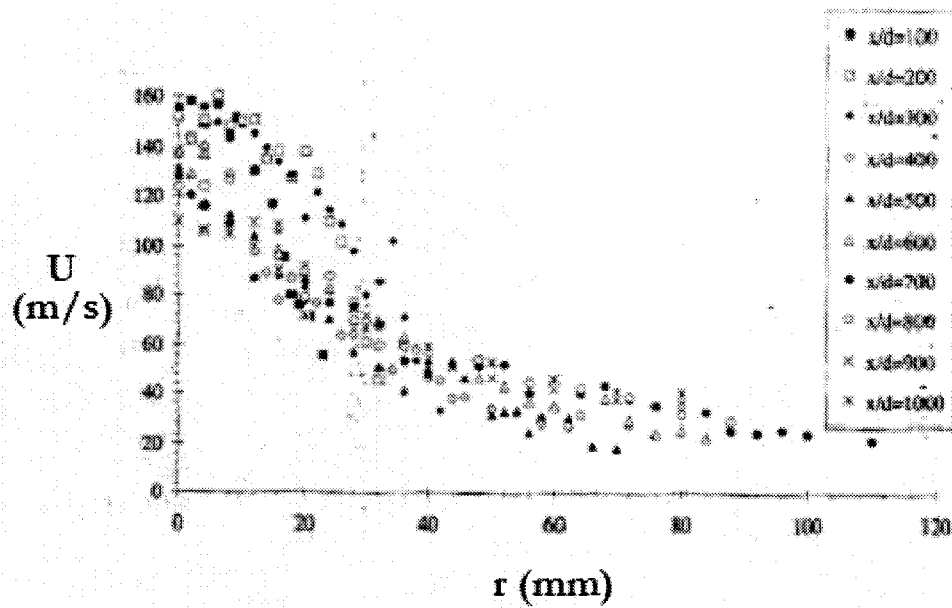
Figure 2.8: Velocity Distribution at Different Axial Locations [Rajaratnam et al.

(1994)]

In their 1998 paper, Rajaratnam et al. also found that the volume fraction of water decreases sharply along the centreline of the jet, being 20% at $20D$ and only 2% at $200D$ (Figure 2.9).
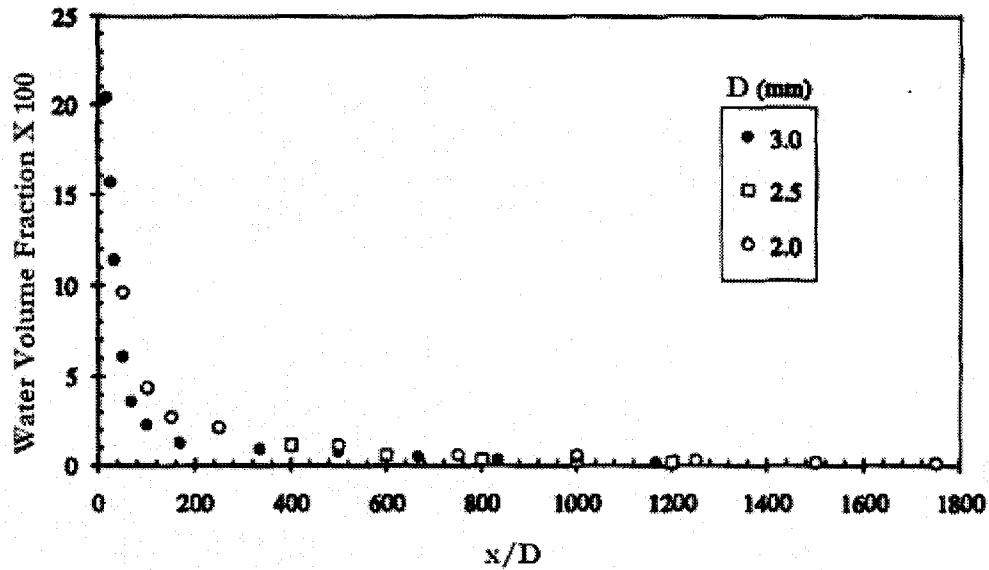
Figure 2.9: Decay of Water Volume Fraction Along the Jet Axis [Rajaratnam et al.

(1998)]

They also measured the volume flow rate of the water phase at different axial and radial locations. If q is the volume flow rate of water and q_m is the corresponding value at the centreline (which is also the maximum value), and b_w is the length scale defined as the radial distance(r) where $q= q_m /2$, then the normalized distribution of q (i.e q/q_m) versus r/b_w could be represented by a Gaussian distribution. They measured the growth of the length scale b_w with axial distance and found the growth rate was 0.005. Unfortunately, they did not provide any figures or data about the radial variation of volume or mass flow rate of the water phase.

Rajaratnam et al. (1998) also mentioned that in these high velocity jets, the momentum flux is carried by both water and air streams, with their relative share varying along the jet. The relative momentum flux carried by the water falls to about 30% at 1600D. Also they found that there is insignificant loss of the mass flux of water in high speed jets. At

an axial distance of 750D, the difference with the inlet mass flux was just 6%, probably in the form of mist.

2.5 Different Regimes of Jet Break-up

Lin et al. (1998) analyzed the break up of liquid jets in air. High speed water jets discharging into quiescent air undergo break-up and atomization. The break-up and spray formation can be attributed to a large number of parameters like nozzle internal flow effects resulting from cavitation, the jet velocity profile and turbulence at nozzle exit, and the physical and thermodynamic states of both the liquid and the ambient air. The jet turbulence contributes to the ruffling of the jet surface, making it prone to break up by aerodynamic effects. Fully turbulent liquid jets may break up by themselves if the turbulence intensities are sufficiently large, without the need of aerodynamics effects. Four main break-up regimes have been identified that correspond to different combinations of liquid inertia, surface tension, and aerodynamic forces acting on the jet. The break-up regimes have been named the Rayleigh regime, the first wind-induced regime, the second wind-induced regime and the atomization regime. At low jet velocities, the growth of long wavelength small amplitude disturbances on the liquid surface prompted by the interaction between the liquid and the ambient gas are believed to initiate the liquid break-up process. For moderate speed liquid jets, the break-up is thought to result from the unstable growth of short wavelength waves. For the Rayleigh and first wind-induced regimes, the drop sizes are comparable with the diameter of the jet, whereas for the second wind-induced and atomization regimes, the drop sizes are very small compared to the jet diameter. For even higher speeds, the jet may break up right at the nozzle exit, producing an atomized jet. All the previous literatures cited are

high speed jets, hence they can be categorized in the atomization regime. Figure 2.10 and

Table 2.1 depicts the classification of liquid jet break-up.
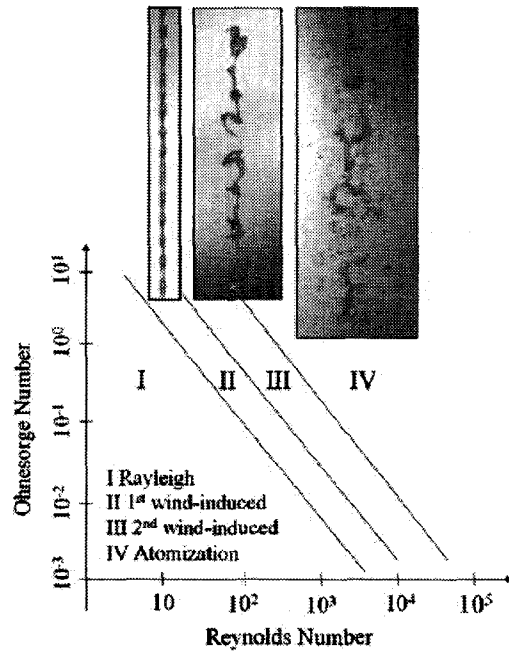
Figure 2.10: Classification of Jet Break-up [Anantharamaiah et al.]

Break-up Region	Condition
Rayleigh break-up region	$We_l > 8$ and $We_g < 0.4$ or $1.2{+}3.41(Oh)^{0.9}$
The first wind-induced region	$1.2{+}3.41(Oh)^{0.9} < We_g < 13$
The second wind-induced region	$13 < We_g < 40.3$
Atomization region	$We_g > 40.3$

Table 2.1: Classification of Jet Break-up [Anantharamaiah et al. (2006)]

In Table 2.1, We is Weber Number, Re is Reynolds Number, Oh is Ohnesorge Number, U_l is jet velocity at nozzle exit, D is nozzle exit diameter, s is surface tension between

16

water and air, ρ is density and μ is viscosity of water. Subscripts are l for liquid and g for gas (air in this case).

These flow parameters are defined as:

$$We_g = \frac{U_l^2 \rho_g D}{s}, \quad We_l = \frac{U_l^2 \rho_l D}{s}, \quad \mathrm{Re}_l = \frac{U_l \rho_l D}{\mu_l}, \quad Oh = \frac{We_l^{0.5}}{\mathrm{Re}_l}$$

This classification doesn't take nozzle internal flow conditions like geometry, cavitation, etc into account. These parameters also have pronounced effect on jet break-up, especially for high speed jets.

2.6 Break-up of High Speed Jets and Sprays

Yoon et al. (2004) did experimental measurements and numerical simulations of high-speed water sprays (80 m/s) emanating from a Rouse type nozzle (See Figure 2.1c) of 2 mm diameter. The numerical model was based on a stochastic separated flow technique that includes sub-models for droplet dynamics, heat and mass transfer, and droplet–droplet collisions. They obtained very good agreement in the comparisons of experimental measurements to computational predictions for the streamwise development of mean drop size and velocity. They argued that the high Weber number (174,387) causes the emanating spray to atomize quickly. It is well known that Rayleigh instability analysis can predict the breakup length for low speed jets (Rayleigh, 1878; Weber, 1931; McCarthy and Molloy, 1974; Sterling and Sleicher, 1975) while the break up of moderate speed jets (Sallam and Faeth, 1999; Sallam et al., 2002; Hoyt and Taylor, 1977a) are also predicted well since the larger wavelengths are affected by Rayleigh instability while the

smaller wavelengths are affected by other instability sources (i.e., Kelvin–Helmholtz type instability, boundary-layer instability, turbulence etc.). However, they argued that the existing methods for estimating jet breakup length is not applicable to very high speed jets where the Weber number (We_l) exceeds 100,000.This is because there are no larger-scale disturbances and small-scale disturbances dominate the flow physics, which cannot be predicted by the Rayleigh type instability analysis. Figure 2.11 shows how Weber number can affect the break-up of liquid jet and how high speed liquid jets significantly differ from moderate velocity liquid jets.
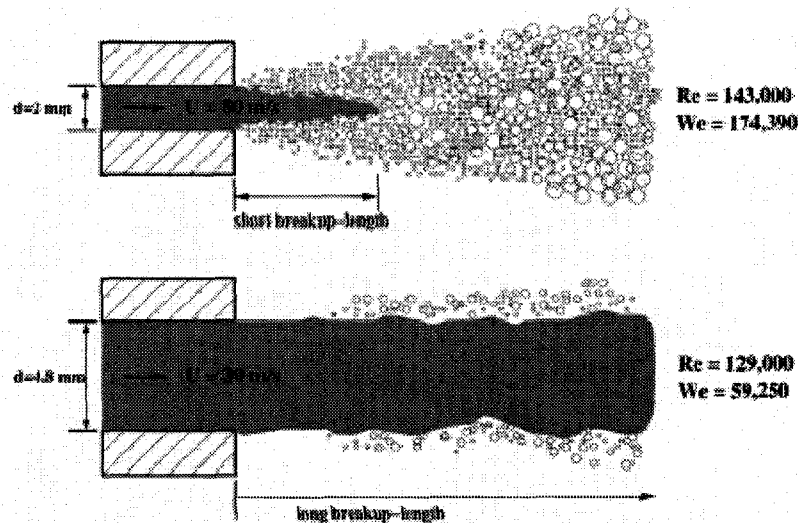
Figure 2.11: Two Different Turbulent Jets at Different Weber Number. (Top) Highly Atomizing Jet with Short Break-Up Length at Very High Weber Number. (Bottom) Moderately Atomizing Jet with Long Break-Up Length at Moderately High Weber Number; The Jet Investigated in Sallam et al. (2002). [Yoon et al. (2004)]

2.7 Effect of Nozzle Cavitation on Jet Characteristics

Hiroyasu et al. (1991), Hiroyasu (2000), Arai et al. (1988), Tamaki et al. (2001), Vahedi et al. (2003) and Sou et al. (2007) have already shown that jet characteristics can be significantly influenced by nozzle cavitation. Varying the nozzle geometry and keeping the injection pressure fixed, water jets can have a long intact length, or can turn into spray right at the nozzle outlet. Similarly, keeping the nozzle geometry fixed and varying injection pressures can produce similar phenomenon as shown by Sou et al. (2007). They proposed that the collapse of cavitation bubbles in the nozzle produces high turbulence intensities along with a lateral velocity component. If the cavitation number is low enough (super cavitation) and the cavitation cloud reaches near the nozzle exit, the collapse of the cavitation cloud causes the jet to spread (because of the lateral velocity component) and break-up right at the nozzle exit (because of higher turbulent intensities). Figure 2.11 shows that the length of the cavitation cloud in the nozzle can significantly affect the emanating jet characteristics.
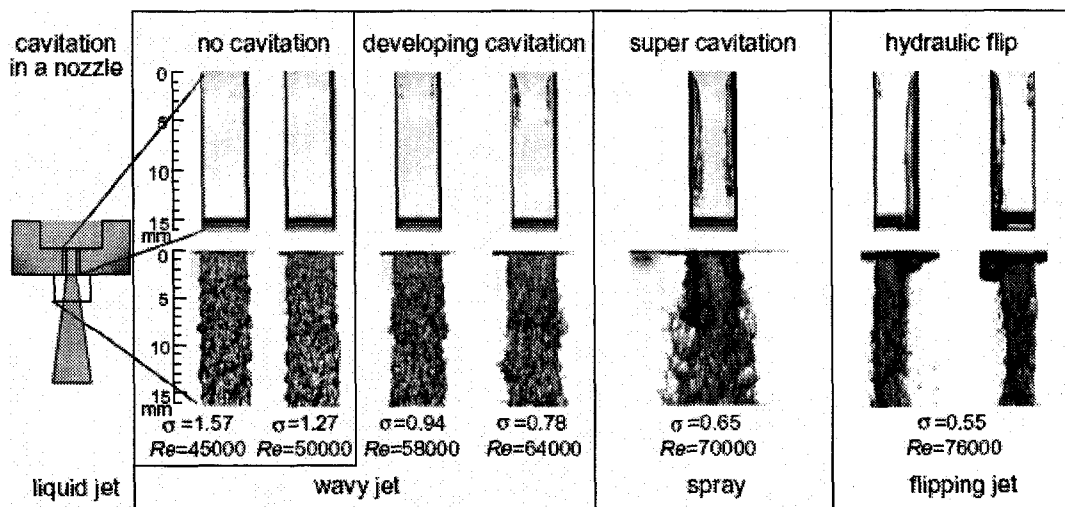
Figure 2.12: Effect of Nozzle Cavitation on Emanating Jet [Sou et al. (2007)]

19

2.8 Overview of Previous Research and Scope for Future Work

From the existing literature we have observed that very high speed turbulent water jets are usually characterized in the atomization regime ($We_g > 40.3$) and have very high Weber Numbers ($We_l > 100,000$). Present instability analyses cannot predict the break-up length of these jets since small-scale disturbances dominate the flow physics. Some experimental work has been done on jet flow characteristics, especially for jets emanating from converging-straight nozzles. It has been found that there are numerous factors like nozzle geometry, cavitation, aerodynamic effects, etc., which can greatly affect the jet characteristics. However, the inclusion of these effects into the jet behaviour is still not possible. Also, there has been no numerical work to characterize the flow physics of high speed jets. For example, the pressure, velocity and volume fraction distributions that have been experimentally obtained have not been numerically modeled. Also, there are several issues with the analysis of the previous experimental works. The analytical curve formulated by Leach et al. (1966) to describe the pressure distribution at the target plate may not be the best fit curve, and the number of experimental data points in their analysis is very limited. The mathematical equation given by Yanaida and Ohashi (1980) to describe the pressure distribution along the jet centreline gives a good fit after $350D$. At a distance of $350D$, the jet looses almost half of its pressure and hence regions as far as this have little or no significance from an application point of view. The experimental works have focused mainly on jets emanating from converging-straight nozzles, which are industrially less popular than converging nozzles. Hence, there is a large scope for both experimental and numerical work in this field.

Of special interest to us, the manufacturing industry uses high speed turbulent jets emanating mainly from converging nozzles. These kinds of jets are extensively used in cleaning of industrial parts. Hence, we focus on those regions of a jet which have sufficient pressure to deliver to the cleaning surface. Our aim is to experimentally observe what the pressure distribution at a target plate, placed at an axial distance near to a converging nozzle, will look like. Since, to the best of our knowledge, no numerical work has been performed on the flow characteristics of high speed jets, our aim will also be to model high speed jet flows and to numerically validate the works of Rajaratnam et al. (1994, 1998) and Leach et al. (1966). Furthermore, we will build a numerical model which can be validated by our own experiments.

Chapter 3

COMPUTATIONAL METHODOLOGIES

3.1 Introduction

The focus of this chapter is to introduce the computational methodologies involved in this research work. The discussion will focus on numerical modeling of turbulent multiphase flows with special attention to the Eulerian multiphase model and the k-ε turbulence model.

3.2 Multiphase Flows [FLUENT MANUAL]

A large number of flows encountered in nature are a mixture of phases. Physical phases of matter are solid, liquid and gas but the concept of phase in a multiphase flow system is applied in a broader sense. In multiphase flow, a phase can be defined as an identifiable class of material that has a particular inertial response to, and interaction with, the flow field in which it is immersed. For example, solid particles of different sizes but of the same material can be treated as different phases because each collection of particles with the same size will have a similar dynamical response to the flow field. Multiphase flows can be grouped into four categories: gas-liquid or liquid-liquid flows; gas-solid flows; liquid-solid flows; and n-phase flows. The focus of our work is on gas-liquid flows. Generally speaking, gas-liquid flows can be divided into the following categories:

Bubbly flow: This is the flow of discrete gaseous or fluid bubbles in a continuous fluid.

Droplet flow: This is the flow of discrete fluid droplets in a continuous gas.

Slug flow: This is the flow of large bubbles in a continuous fluid.

Stratified/free-surface flow: This is the flow of immiscible fluids separated by a clearly-defined interface.

3.3   Modeling of Multiphase Flows [FLUENT MANUAL]

Advancement in the field of computational fluid dynamics have provided the basis for further insight into the dynamics of multiphase flows. Currently there are two approaches for the numerical calculation of multiphase flows: the Euler-Lagrange approach and the Euler-Euler approach. The Euler-Lagrange approach is based on tracking of the dispersed secondary phase. The basic assumption of this model is that the secondary phase occupies a very low volume fraction compared to the primary phase. Hence this model is not suitable for modeling high speed jet flows since, in these flows, the volume fraction of air (secondary phase) is not low compared to the volume fraction of water (primary phase). In the Euler-Euler approach, the different phases are treated mathematically as interpenetrating continua. Since the volume of one phase cannot be occupied by the other phases, the concept of phasic volume fraction is introduced. These volume fractions are assumed to be continuous functions of space and time and their sum is equal to one. Conservation equations for each phase are derived to obtain a set of equations, which have similar structure for all phases. These equations are closed by providing constitutive relations that are usually obtained from empirical information. In FLUENT, three different Euler-Euler multiphase models are available: the volume of fluid (VOF) model, the mixture model, and the Eulerian model.

The VOF Model: The VOF model is a surface-tracking technique applied to a fixed Eulerian mesh. The model is designed for two or more immiscible fluids where the position of the interface between the fluids is of primary interest. In the VOF model, a single set of momentum equations is shared by the fluids, and the volume fraction of each of the fluids in each computational cell is tracked throughout the domain.

The Mixture Model: The mixture model is designed for two or more phases (fluid or particulate). All phases are treated as interpenetrating continua. The mixture model solves the mixture momentum equation and prescribes relative velocities to describe the individual dispersed phases. The mixture model can also be used without relative velocities for the dispersed phases to model homogeneous multiphase flow.

The Eulerian Model: The Eulerian model is the most complete and complex of the multiphase models in FLUENT. It solves a set of momentum and continuity equations for each phase. Coupling is achieved through the pressure and interphase exchange coefficients. The method in which this coupling is handled depends upon the type of phases involved. Momentum exchange between the phases is also dependent upon the type of mixture being modeled. FLUENT's user-defined functions (UDF) allow customizing the calculation of the momentum exchange. Because of these features, we have chosen the Eulerian model to simulate our multiphase flow problem.

3.4 Eulerian Multiphase Model in FLUENT [FLUENT MANUAL]

The key features of the FLUENT Eulerian Multiphase Model are:

a)   A single pressure is shared by all phases.

b)   Momentum and continuity equations are solved for each phase.

c)   Several inter-phase drag coefficient functions are available, which are appropriate for various types of multiphase regimes.

d)   Three k-ε turbulence models are available, and may apply to all phases or to the mixture.

To change from a single-phase model, where a single set of conservation equations for momentum, continuity and (optionally) energy is solved, to a multiphase model, additional sets of conservation equations must be introduced. In the process of introducing additional sets of conservation equations, the original set must also be modified. The modifications involve, among other things, the introduction of the phasic volume fractions α_1, α_2, ..., α_n for the multiple phases, as well as mechanisms for the exchange of momentum, heat and mass between the phases. Volume fractions represent the space occupied by each phase, and the laws of conservation of mass and momentum are satisfied by each phase individually. The derivation of the conservation equations can be done by ensemble averaging the local instantaneous balance for each of the n phases, or by using the mixture theory approach. The volume of phase i is defined as

$$V = \int_V \alpha_i dV \qquad (3.1)$$

where
$$\sum_{i=1}^{n} \alpha_i = 1 \tag{3.2}$$

The Continuity Equation for phase i is:

$$\frac{\partial(\alpha_i \rho_i)}{\partial t} + \nabla \cdot (\alpha_i \rho_i \vec{v}_i) = \sum_{i=1}^{n} (\dot{m}_{j \to i} - \dot{m}_{i \to j}) + S_i \tag{3.3}$$

where v_i is the velocity of phase i, $\dot{m}_{i \to j}$ is the mass transfer from i phase to j phase and

S_i is the mass source term.

The Momentum Equations for the phase i are:

$$\frac{\partial(\alpha_i \rho_i \vec{v}_i)}{\partial t} + \nabla \cdot (\alpha_i \rho_i \vec{v}_i \vec{v}_i) = -\alpha_i \nabla p + \nabla \cdot \overline{\overline{\tau}}_i + \alpha_i \rho_i \vec{g} +$$

$$\sum_{i=1}^{n} \left\{ K_{ij} (\vec{v}_i - \vec{v}_j) + \dot{m}_{j \to i} \vec{v}_{j \to i} - \dot{m}_{i \to j} \vec{v}_{i \to j} \right\} + \vec{F}_{i,body} + \vec{F}_{i,lift} + \vec{F}_{i,vm} \tag{3.4}$$

where

∇p = pressure gradient

$\overline{\overline{\tau}}_i$ = stress-strain tensor of phase i, given by

$$\overline{\overline{\tau}}_i = \alpha_i \mu_i \left(\nabla \vec{v}_i + \nabla \vec{v}_i^T \right) + \alpha_i \left(\lambda_i - \frac{2}{3} \mu_i \right) \nabla \cdot \vec{v}_i \overline{\overline{I}} \tag{3.5}$$

where μ_i and λ_i are the shear and bulk viscosity of phase i, respectively, and

$\vec{F}_{i,body}$ = external body force

$\vec{F}_{i,lift}$ = lift force = $-0.5 \alpha_j \rho_i (\vec{v}_i - \vec{v}_j) \times (\nabla \times \vec{v}_i)$ \hfill (3.6)

$\vec{F}_{i,vm}$ = virtual mass force = $-0.5 \alpha_j \rho_i \left(\dfrac{D_i}{Dt} \vec{v}_i - \dfrac{D_j}{Dt} \vec{v}_j \right) \times (\nabla \times \vec{v}_i)$ \hfill (3.7)

and $\dfrac{D_i}{Dt} \phi = \dfrac{\partial \phi}{\partial t} + (\vec{v}_i \cdot \nabla) \phi.$ \hfill (3.8)

If $\dot{m}_{i\to j} > 0$, then $\vec{v}_{i\to j} = \vec{v}_j$, and if $\dot{m}_{i\to j} < 0$, $\vec{v}_{i\to j} = \vec{v}_i$.

$$K_{ij}(\vec{v}_i - \vec{v}_j) = \text{interphase interaction force} \tag{3.9}$$

where K_{ij} is the interphase momentum exchange coefficient.

For fluid-fluid flows, each secondary phase is assumed to form droplets or bubbles. This has an impact on how each of the fluids is assigned to a particular phase. For example, in flows where there are unequal amounts of two fluids, the predominant fluid should be modeled as the primary fluid, since the sparser fluid is more likely to form droplets or bubbles. The exchange coefficient for these types of bubbly, liquid-liquid or gas-liquid mixtures can be written in the following general form:

$$K_{ij} = \frac{\alpha_i \alpha_j \rho_j f}{\tau_j} \tag{3.10}$$

where f is the drag function and τ_j is the particulate relaxation time, defined as

$$\tau_j = \frac{\rho_j d_j^2}{18\mu_i} \tag{3.11}$$

where d_j is the diameter of droplets or bubbles of phase j. In our work we have used the Schiller and Naumann model to evaluate the drag function as follows:

$$f = \frac{C_D \text{Re}_{rel}}{24} \tag{3.12}$$

where C_D is the drag coefficient, defined as

$$C_D = \begin{cases} \dfrac{24(1 + 0.15\text{Re}_{rel}^{0.687})}{\text{Re}_{rel}} & \text{Re}_{rel} \leq 1000 \\ 0.44 & \text{Re}_{rel} > 1000 \end{cases} \tag{3.13}$$

where Re_{rel} is the Relative Reynolds Number, defined as

$$\text{Re}_{rel} = \frac{\rho_i \left|\vec{v}_i - \vec{v}_j\right| d_j}{\mu_i} \tag{3.14}$$

3.5   Standard *k-ε* Turbulence Model in FLUENT [FLUENT MANUAL]

FLUENT provides three methods for modeling turbulence in multiphase flows within the context of the *k-ε* models. In addition, FLUENT provides two turbulence options within the context of the Reynolds Stress Models (RSM). The *k-ε* turbulence model options are a) mixture turbulence model, b) dispersed turbulence model and, c) turbulence model for each phase. In our modeling, we have used the mixture turbulence model. The *k-ε* transport equations for this model are as follows:

$$\frac{\partial(\rho_m k)}{\partial t} + \nabla \cdot \left(\rho_m k \vec{v}_m\right) = \nabla \cdot \left(\frac{\mu_{t,m}}{\sigma_k} \nabla k\right) + G_{k,m} - \rho_m \varepsilon \tag{3.15}$$

$$\frac{\partial(\rho_m \varepsilon)}{\partial t} + \nabla \cdot \left(\rho_m \varepsilon \vec{v}_m\right) = \nabla \cdot \left(\frac{\mu_{t,m}}{\sigma_\varepsilon} \nabla \varepsilon\right) + \frac{\varepsilon}{k}(C_{1\varepsilon} G_{k,m} - C_{2\varepsilon} \rho_m \varepsilon) \tag{3.16}$$

where the mixture density (ρ_m) and mixture velocity ($\vec{v}_m$) are computed as:

$$\rho_m = \sum_{i=1}^{n} \alpha_i \rho_i \tag{3.17}$$

$$\vec{v}_m = \frac{\sum_{i=1}^{n} \alpha_i \rho_i \vec{v}_i}{\sum_{i=1}^{n} \alpha_i \rho_i} \tag{3.18}$$

The turbulent viscosity ($\mu_{t,m}$) and the production of turbulent kinetic energy ($G_{k,m}$) are calculated as follows:

$$\mu_{t,m} = \rho_m C_\mu \frac{k^2}{\varepsilon} \qquad (3.19)$$

$$G_{k,m} = \mu_{t,m}\left(\nabla\vec{v}_m + (\nabla\vec{v}_m)^T\right) \qquad (3.20)$$

The values of the model constants are taken as the "standard" values $C_{1\varepsilon} = 1.44$, $C_{2\varepsilon} = 1.92$, $C_\mu = 0.09$, $\sigma_k = 1.0$, $\sigma_\varepsilon = 1.3$. Standard wall functions were used to model near wall flows. For brevity, the description of standard wall functions is not discussed. Interested readers can refer to FLUENT documentation for details.

Chapter 4

NOVEL EMPIRICAL MASS FLUX MODELS TO SIMULATE HIGH SPEED WATER JETS IN AIR

4.1 Introduction

To the best of our knowledge, numerical modeling of high speed water jets in air and validation with experimental results has not been reported in the literature. In this chapter, our aim is to build a numerical model that can characterize the physics of high speed water jets in air and also to compare our model with the existing experimental works of Rajaratnam et al. (1994, 1998) and Leach et al. (1966). High speed water jets diffuse in the surrounding atmosphere by the process of mass and momentum transfer. Air is entrained into the jet stream and the whole process contributes to the spreading of the jet and subsequent decay of pressure. Hence the physical problem is in the category of multiphase flows and in order to model the problem, mass and momentum transfer is to be determined. The Eulerian multiphase model solves each phase separately and hence is most likely the best multiphase model, if computational time is not a constraint. Thus, using the Eulerian multiphase model, we have developed two novel numerical models for mass and momentum transfer which can accurately predict the flow physics of high speed water jets in air.

4.2 Formulation of a Novel Empirical Eulerian Mass Flux Model

As per the studies of Leu et al. (1998), the core and the water droplet zones (Figure 2.1) are of prime importance for industrial cleaning since these zones have significant

momentum to deliver to the cleaning surface. Yanaida et al. (1980) analyzed the core and the water droplet zone together and divided the jet flow according to radial distance from the centreline (see Figure 2.5). The inner region is the continuous flow region, the radial width of which varies as

$$R_{inner} = k_1 \sqrt{xR_0}$$ (4.1)

Outside of this region is the droplet flow region, the radial width of which varies as

$$\frac{dR_{outer}}{dx} = \frac{C}{R_0}$$ (4.2)

where k_1 and C are Spread Coefficients and are related as $C = \dfrac{k_1}{1.9}$. (4.3)

According to Erastov's experiment (Abramovich, 1963), the mass flow rate in these water jets have the following relationship:

$$\frac{\dot{M}(x,r)}{\dot{M}(x,0)} = \left\{ 1 - \left(\frac{r}{R}\right)^{1.5} \right\}^3$$ (4.4)

where $\dot{M}$ is the mass flux (in the axial direction) of water droplets (kg/m^{2}s), r is the radial coordinate of a point in the jet, and R is either R_{inner} or R_{outer} depending on the radial location. Also, for a fluid, we can write

$$\dot{M}(x,r) = \alpha_w(x,r) \times \rho_w \times V_w(x,r)$$ (4.5)

where α_w (x,r) and V_w(x,r) are the volume fraction and axial velocity of water droplets at location (x,r) respectively. According to the conservation of mass principle, the mass flow rate at any cross-section of the jet is equal to the mass flow rate at the nozzle exit (Leu et al., 1998). If the droplet flow is assumed to be a continuum, then this principle can be represented as

$$\dot{M}_0 \pi (R_0)^2 = 2\pi \int_0^R \dot{M}(x,r) r \, d(r) \tag{4.6}$$

where R_0 is the nozzle radius. Using Equation (4.4) in (4.6), a relation between the centreline mass flux and the nozzle exit mass flux was obtained as follows:

$$\dot{M}(x,0) = \frac{5.62 \dot{M}_0 R_0{}^2}{R^2} \tag{4.7}$$

The mass flux of water droplets at any point in the jet can be expressed in terms of nozzle exit mass flux by substituting Equation (4.4) in (4.7). The relation is given by

$$\dot{M}(x,r) = \frac{5.62 \dot{M}_0 R_0{}^2}{R^2} \left\{ 1 - \left(\frac{r}{R} \right)^{1.5} \right\}^3 \tag{4.8}$$

Substituting Equation (4.5) in (4.8)

$$\dot{M}(x,r) = \rho_w \times \alpha_w(x,r) \times V_w(x,r) = \frac{5.62 \times \rho_w \times \alpha_0 \times V_0 \times R_0{}^2}{R^2} \left\{ 1 - \left(\frac{r}{R} \right)^{1.5} \right\}^3 \tag{4.9}$$

where α_0 and V_0 are the volume fraction and velocity of water at nozzle exit respectively. At the nozzle exit, the volume fraction of water is 100%.

Equation (4.9) is the polynomial function based empirical mass-flux model. If the nozzle exit velocity is properly known, this model can be used to estimate the flow characteristics of high speed water jets in air.

4.3 Preliminary Validation of the Mass Flux Model

Before implementing the mass flux model numerically, we wanted to examine whether the model is good enough for numerical implementation. Looking at Equation (4.9), we see that there are two unknowns, volume fraction α_w *(x,r)* and velocity *V_w(x,r)*. Solving Equation (4.9) together with the Navier-Stokes equations will give solutions for both the unknowns. But for preliminary comparison with experimental results, we will restrict ourselves to an analytical study. This means that we have only one equation (Equation 4.9) and two unknowns. As it is not possible to solve both the unknowns by one equation, one of them should be known beforehand. Fortunately, from the experimental results of Rajaratnam et al. (1994), we know that the jet centreline velocity remains equal to the nozzle exit velocity up to around $150D$ (i.e. $V(x,0) = V_0$), so Equation (4.9) can be reduced to only one unknown α_w. Thus within $x = 150D$, we can write

$$\alpha_w(x,0) = \frac{5.62\alpha_0 R_0^{\,2}}{R_{inner}^2} \tag{4.10}$$

Since this is centreline characteristics, r has been set to zero and R to R_{inner}. Figure 4.1 shows that the centreline water volume fraction decay is predicted very accurately by this analytical model.
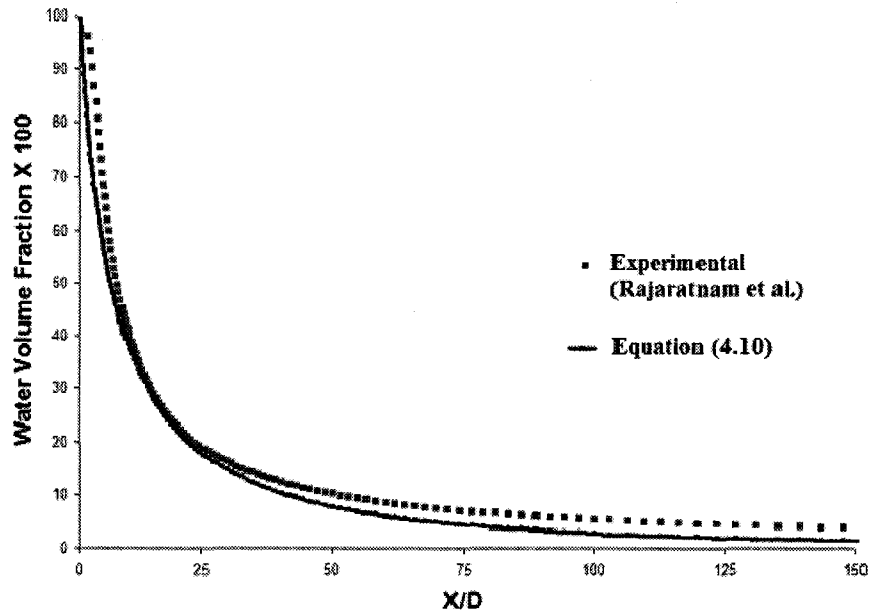
Figure 4.1: Water-Phase Volume Fraction along the Jet Centreline According to Equation (4.10) and Comparison with Experimental Results of Rajaratnam et al. (1998)

As the analytical study has shown very good results, it is worth testing Equation (4.9) numerically. If implemented numerically, there are a sufficient number of equations to solve all the flow variables and thus there is no need to impose any restrictions like that done in this analytical study. Thus, the volume fraction along the centreline can be solved for $x > 150D$ and other flow variables like velocity and pressure can be numerically obtained and can be compared with experimental results.

4.4 Numerical Modeling

In order to obtain both the volume fraction and velocity distribution of this water-air multiphase flow problem in the entire domain of the jet flow, the empirical mass flux

model (Equation (4.9)) must be coupled with the continuity and momentum equations for multiphase flows. The computational domain and structured grid system were created in GAMBIT. Since the problems under consideration involve circular jets, only half of the domain was simulated in a two-dimensional axisymmetric space. The computational space was taken to be 1000 mm × 500 mm, and a tightly clustered grid was ensured in the regions where larger flow gradients are expected. The radial extent of the domain was large enough to ensure that the pressure outlet boundary condition (set at atmospheric pressure) and the wall boundary conditions can be accurately applied, i.e., without adversely affecting the flow field.
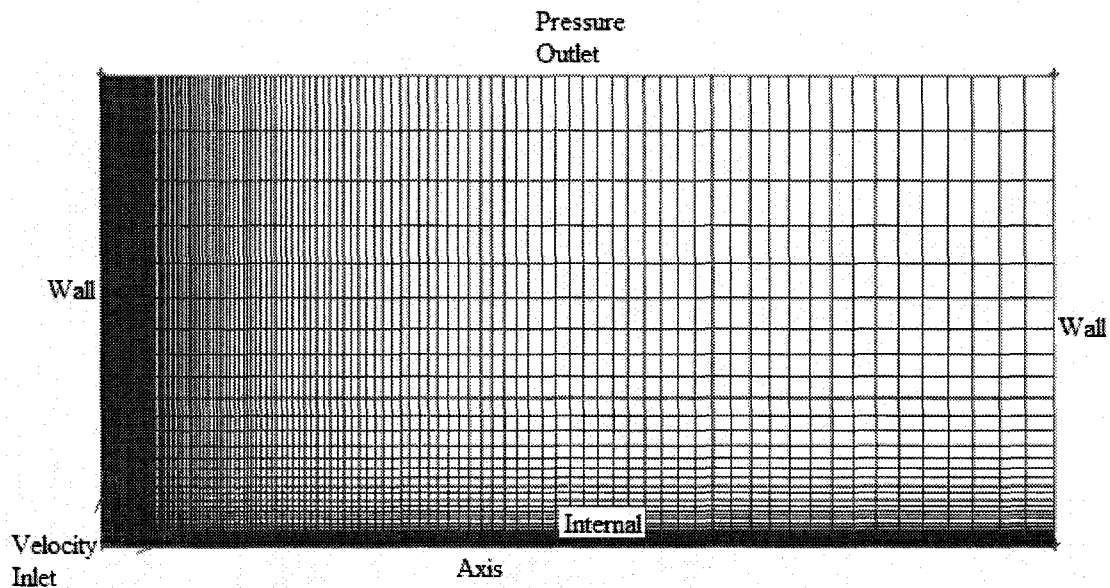
Figure 4.2: Boundary Conditions, Geometry and Meshing

The flow domain was divided into two parts by introducing an internal boundary condition. This enables the specification of different mesh distributions in the two parts. The part near the axis was formed with cells of uniform radial length of 0.1 mm. This small spacing is essential to accurately capture the mass transfer. In the other region, the

35

largest radial length of the grid was 1.5 mm, located at the pressure outlet boundary. There was a gradual decrease in the radial length of the cells by a successive ratio of 0.93. This produced a very fine grid (~ 0.1-0.2 mm) in the region where the jet-air interface was expected. A velocity inlet boundary condition was imposed as the inlet condition. The radial width of the inlet was 1 mm.

FLUENT was used as the flow solver. The Eulerian multiphase model and standard k-ε turbulence model with standard wall functions were used to capture the flow physics. Water was treated as the secondary phase. The drag coefficient between the phases was determined by the Schiller-Naumann equation (see Chapter 3 for details of these models). The continuity and momentum equations respectively for the w (water) phase in the Eulerian model for multiphase flows are, respectively (elaborated in Chapter 3)

$$\frac{\partial(\alpha_w \rho_w)}{\partial t} + \nabla \cdot (\alpha_w \rho_w \vec{v}_w) = \sum_{i=w,a} (\dot{m}_{a \to w} - \dot{m}_{w \to a}) + S_w \tag{4.12}$$

$$\frac{\partial(\alpha_w \rho_w \vec{v}_w)}{\partial t} + \nabla \cdot (\alpha_w \rho_w \vec{v}_w \vec{v}_w) = -\alpha_w \nabla p + \nabla \cdot \bar{\bar{\tau}}_w + \alpha_w \rho_w \vec{g} +$$

$$\sum_{i=w,a} \left\{ K_{wa}(\vec{v}_w - \vec{v}_a) + \dot{m}_{a \to w} \vec{v}_{a \to w} - \dot{m}_{w \to a} \vec{v}_{w \to a} \right\} + \vec{F}_w \tag{4.13}$$

The term $\dot{m}_{w \to a}$ is the mass transfer from w (water) phase to a (air) phase. In the physical problem, the surrounding air is entrained into the jet and the mass of air in the jet increases. To implement this process numerically, we set $\dot{m}_{a \to w}$ and S_w as zero, leaving $\dot{m}_{w \to a}$ as the only mass source term in the right hand side of Equation (4.12). Since the mass flux of the water phase at all the points in the domain is known from the empirical mass flux model (Equation (4.9)), we incorporate it into the continuity equation (4.12) as follows:

$$\dot{m}_{w \to a} = \nabla \cdot (\dot{M}, 0) \tag{4.14}$$

The source term due to momentum transfer ($\dot{m}_{w \to a}\vec{v}_{w \to a}$) in Equation (4.13) is automatically handled by FLUENT once the mass transfer is specified. The incorporation of Equation (4.14) in the continuity equation is accomplished using User Defined Functions (UDF) in FLUENT.

Pressure-velocity coupling was achieved using the phase-coupled SIMPLE algorithm. All the residuals tolerances were set to 10^{-6} and the time step size was 10^{-5} seconds. The program was run for a time long enough to attain quasi-steady state. The default under-relaxation parameters of FLUENT were used in the computation. The discretization schemes used in the simulation are listed below.

Variables	Discretization Scheme
Time	First Order implicit
Momentum	QUICK
Volume Fraction	QUICK
Turbulent Kinetic Energy	Second Order Upwind
Turbulent Dissipation Rate	Second Order Upwind

Table 4.1: Discretization Schemes for Jet Flow

4.5 Results

Results obtained by this model are shown below. Figure 4.3 confirms that the empirical mass flux model is correctly incorporated in FLUENT, thus the numerical centreline water volume fraction decay matches very well with the experimental work of Rajaratnam et al. (1998). Figure 4.4 shows that the constant behaviour (up to around

150D) as well as the linear decay of the centreline velocity beyond 150D are also predicted very accurately with this model (up to 400D is shown).
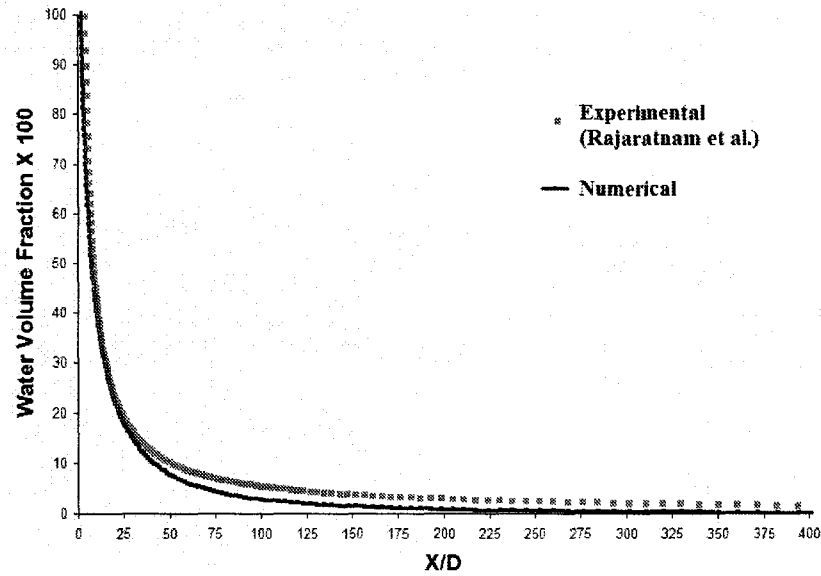
Figure 4.3: Numerical Simulation of the Decay of Centreline Water Phase Volume Fraction and Comparison with Experimental Results of Rajaratnam et al. (1998)
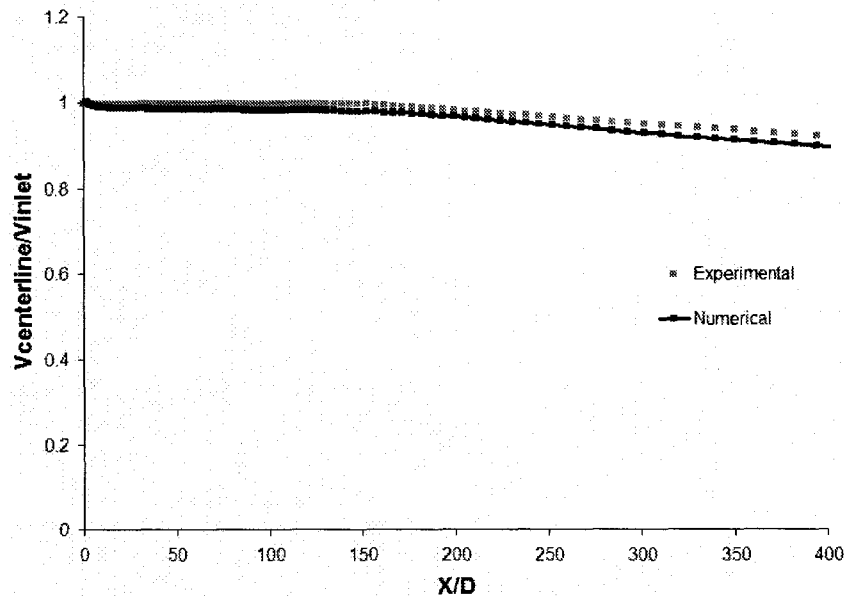
Figure 4.4: Numerical Simulation of Centreline Water Phase Velocity and Comparison with Experimental Results of Rajaratnam et al. (1994)

The velocity profiles for x/D=100, 200 and 300 are shown in Figure 4.5 and the normalized profiles (w.r.t centreline velocity) are shown in Figure 4.6. Good match with the experimental results is obtained up to r/D=5.
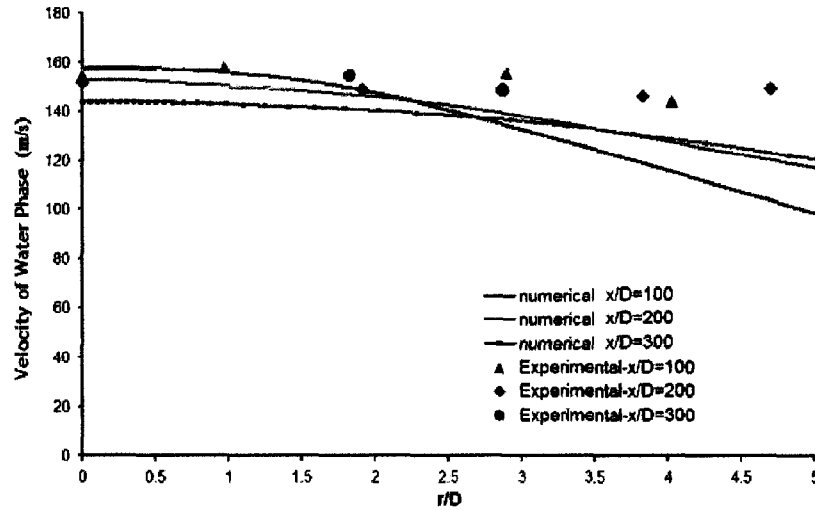
Figure 4.5: Velocity Distribution at x/D=100,200,300 and Comparison with

Experimental Results of Rajaratnam et al. (1994)
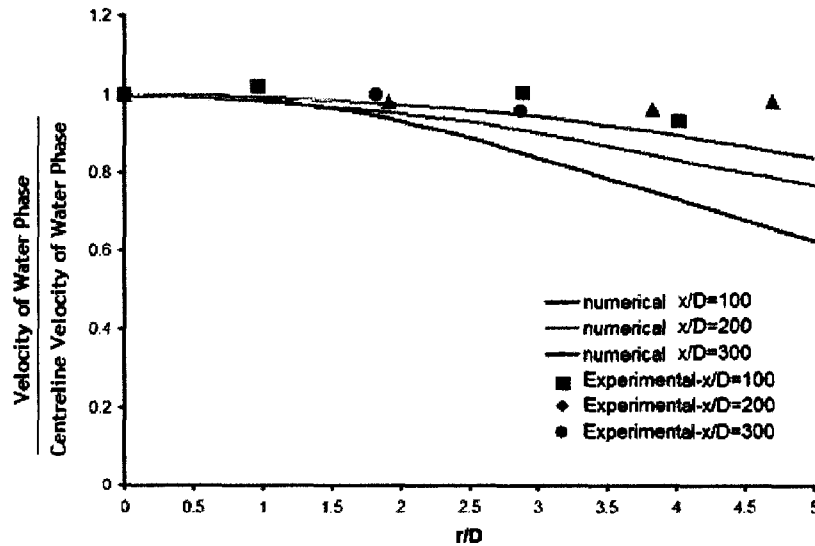
Figure 4.6: Normalised Velocity Distribution at x/D=100,200,300 and

Comparison with Experimental Results of Rajaratnam et al.(1994)

Thus from the obtained numerical results, we can conclude that the model gives an excellent match to the experimental work of Rajaratnam et al.(1994,1998).

Figure 4.7: Contour of Water Phase Volume Fraction in the Jet (within x/D=10)
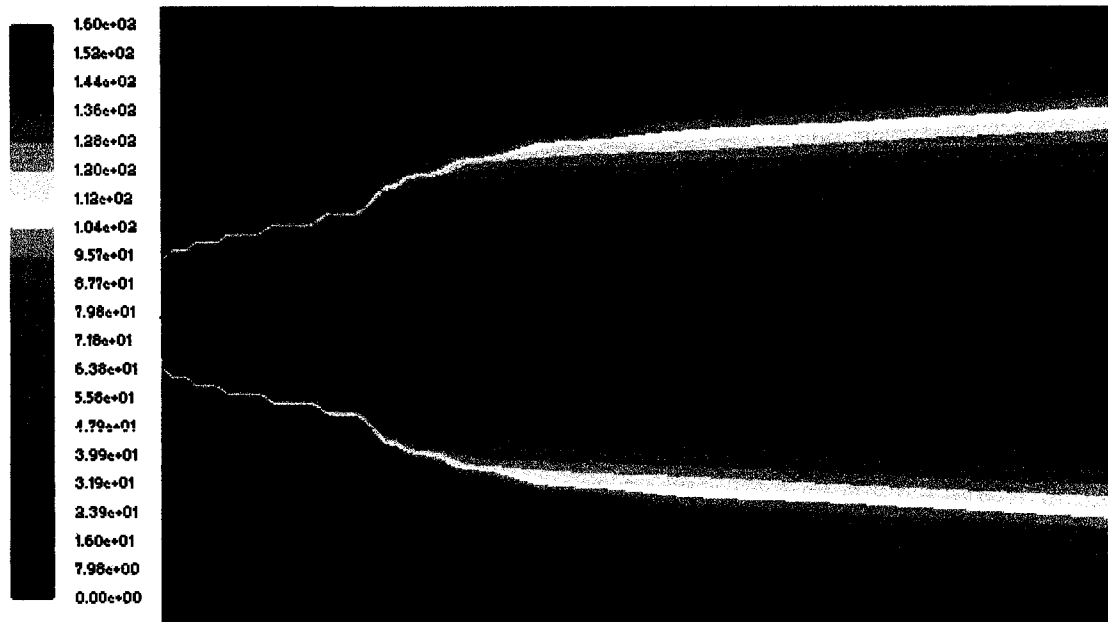
Figure 4.8: Contour of Water Phase Velocity in the Jet (within x/D=10)

Figures 4.7 and 4.8 show the velocity and volume fraction contours of the water phase up to $x/D = 10$. The figures are drawn to the same geometric scale, giving a quantitative comparison between the two contours. The volume fraction contour shows that the water phase volume fraction decays sharply with increased radial distance while the velocity contour shows that the velocity magnitude remains almost constant for considerable radial distance. The velocity contour is much wider than the volume fraction contour. This observation is in congruence with Rajaratnam et al. (1998) but they did not provide with the results of volume fraction distribution in the radial direction. Thus it can be concluded that a considerable amount of air is entrained within the jet. Near the outer region of the jet, the co-flowing air carries the water droplets (of negligible volume fraction) and has considerably high velocity. Near the centreline, the entrained air has a relatively high volume fraction (which increases radially) and it moves with the same velocity as the water phase.

We are particularly interested to assess how the model works in predicting the radial pressure distribution at a target plate placed in the flow field of the jet. Experimental work on this was done by Leach et al. (1966) using a 1 mm diameter nozzle having nozzle velocity and pressure of 350 m/s and 60 MPa respectively. They also obtained an analytical curve to fit their experimental data. In order to simulate their experiment with our analytical mass flux model, we modified the computational domain as shown in Figure 4.9. The figure shows the computational domain with the boundary conditions and meshing.
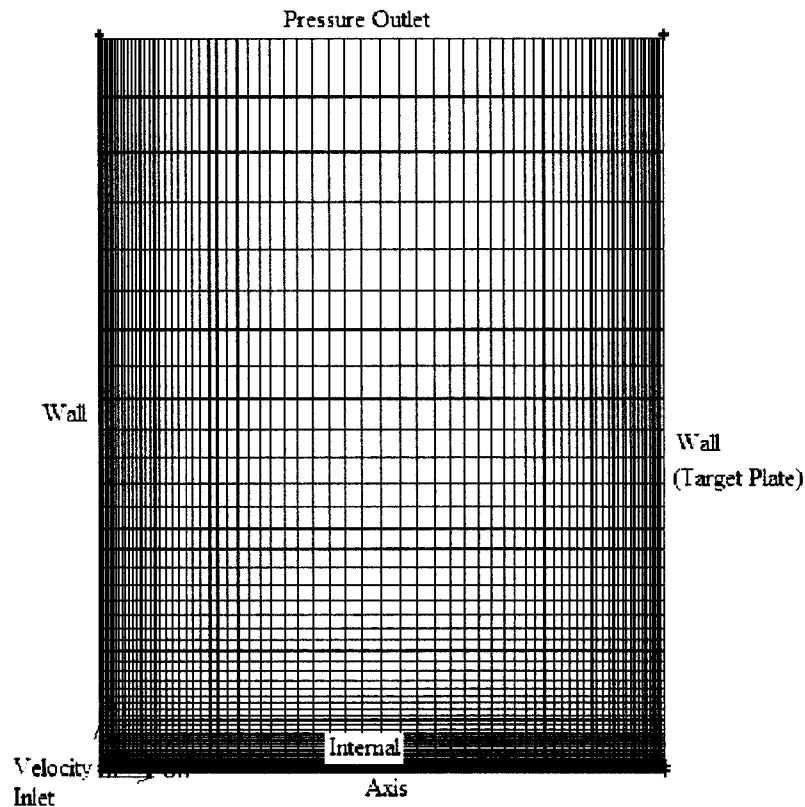
Figure 4.9: Boundary Conditions, Geometry and Meshing

Since this nozzle and resulting jet are also circular, only half of the domain was simulated in a two-dimensional axisymmetric space. The boundary conditions were similar to those implemented in the numerical simulation done to validate Rajaratnam et al. (1994, 1998). In this case, the domain was set to be 76 mm X 250 mm and the inlet width was 0.5 mm. Unlike the previous computational domain, this domain has tighter meshing at the target plate (wall boundary) in order to capture large pressure gradients. Two way clustering was done, i.e., maximum axial grid length was 2 mm at the middle of the domain and decreased in both directions by a successive ratio of 0.93. This ensured clustering at both the nozzle exit and the target plate.

Figure 4.10 shows the pressure at the target, normalized by the target pressure at the centreline. The target was placed at 76D from the nozzle exit. Comparison of our model with the results of Leach et al. (1966) shows good match.
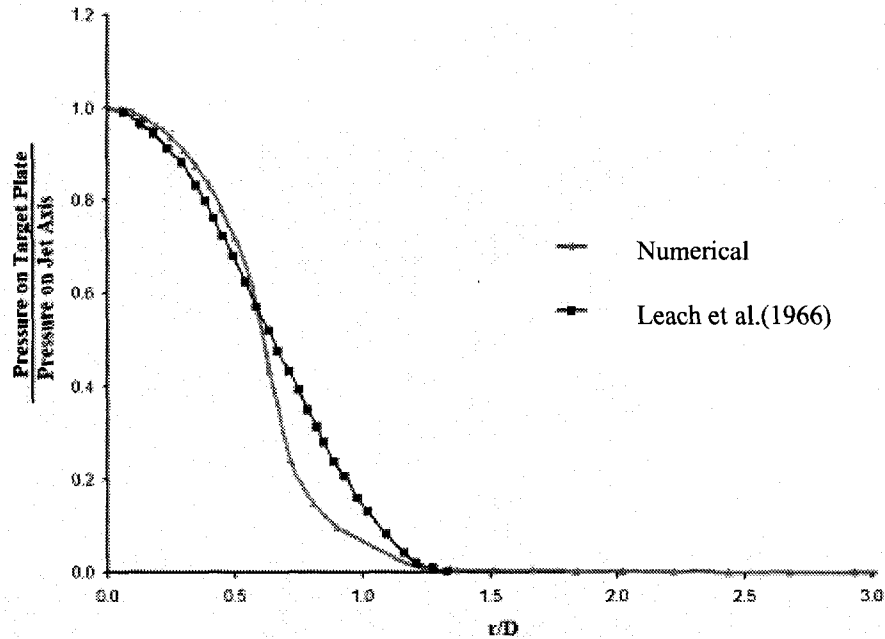
Figure 4.10: Normalized Pressure Distribution on a Target Plate placed at 76D and

Comparison with Leach et al. (1966)

4.6   A Second Approach

An alternate form of the empirical mass flux model derived in Equation (4.9) can also be obtained. The previous model was based on Erastov's normalised mass flux equation (Equation (4.4)) and he assumed that the normalized mass flux varies with the

normalized radial distance according to a particular polynomial function. In this new approach, we replace this polynomial function by a Gaussian distribution.

Rajaratnam et al. (1994) found that the width of the jet (R) increases linearly with axial distance by a growth rate of 0.07 . Thus

$$\frac{dR}{dx} = 0.07 \qquad (4.15)$$

They also measured the volume flow rate of the water phase at different axial and radial locations. If q is the volume flow rate of water, q_m is the corresponding value at the centreline (which is also the maximum value), and b_w is the length scale defined as the radial distance(r) where $q = q_m/2$, then the normalized distribution of q (i.e q/q_m) versus r/b_w could be represented by a Gaussian distribution. It is to be noted here that the volume flow rate corresponding to a point was actually measured over a small area (3.14 mm^2).They found that this distribution is similar even at regions near the nozzle exit. They also measured the growth of the length scale b_w with axial distance and found a growth rate of 0.005. Thus

$$\frac{db_w}{dx} = 0.005 \qquad (4.16)$$

Although they inferred that the q/q_m versus r/b_w could be represented by a Gaussian distribution, they haven't provided with any figure, equation or data for it. Thus our aim will be to derive the Gaussian distribution and then to build a mass flux model that can validate their experimental results. Since q/q_m versus r/b_w follows a Gaussian distribution, the normalized mass flux of water phase $\left(\dot{M}(x,\frac{r}{b_w})/\dot{M}(x,0) \right)$ versus r/b_w should also follow a Gaussian distribution and can be represented in a general form as

$$\frac{\dot{M}(x,\frac{r}{b_w})}{\dot{M}(x,0)} = A\exp\left(-\frac{\left(\frac{r}{b_w}\right)^2}{2\sigma^2}\right) \qquad (4.17)$$

where $\dot{M}$ is the mass flux of water droplets (kg/m^{2}s), r is the radial coordinate of a point

in the jet, σ is the standard deviation of the Gaussian distribution and A is the amplitude.

The radial co-ordinate is normalized by b_w while the axial is normalized by unity.

Now, the conditions satisfying Equation (4.17) are

$$\frac{\dot{M}(x,\frac{r}{b_w})}{\dot{M}(x,0)} = \frac{1}{2} \text{ at } r/b_w=1 \quad \text{and} \quad \frac{\dot{M}(x,\frac{r}{b_w})}{\dot{M}(x,0)} = 1 \text{ at } r/b_w=0.$$

Using these relations we obtain $A = 1$ and $\sigma = 0.84932$. Thus, Equation (4.17) can be

written as

$$\frac{\dot{M}(x,\frac{r}{b_w})}{\dot{M}(x,0)} = \exp\left(-0.693\left(\frac{r}{b_w}\right)^2\right) \qquad (4.18)$$

Following the same set of steps used to derive the polynomial function based empirical

mass flux model, we deduce the Gaussian distribution based analytical mass flux model

as follows:

$$\dot{M}(x,\frac{r}{b_w}) = \dot{M}_0 0.693\left(\frac{R_0}{b_w}\right)^2\left[1-\exp\left(-0.693\left(\frac{R}{b_w}\right)^2\right)\right]^{-1}\exp\left(-0.693\left(\frac{r}{b_w}\right)^2\right) \qquad (4.19)$$

Like Equation (4.10), we derive the centreline water phase volume fraction using this

Gaussian distribution based analytical mass flux model. As in Section 4.3, the analytical

study was limited to an axial distance of 150D since within this distance, the velocity of

the jet along the centreline remains constant (i.e. $V(x,0) = V_0$). The resulting equation is as follows:

$$\alpha_w(x,0) = \alpha_0 \, 0.693 \left(\frac{R_0}{b_w}\right)^2 \left[1 - \exp\left(-0.693\left(\frac{R}{b_w}\right)^2\right)\right]^{-1} \tag{4.20}$$

Figure 4.11 shows the comparison between Equations (4.10) and (4.20) and the experimental results. It can be readily seen that although Equation (4.20) matches very well with the experimental results, yet Equation (4.10) gives an even better match. Hence, we have not incorporated the Gaussian distribution based analytical mass flux model into FLUENT to solve the flow field in the entire domain.
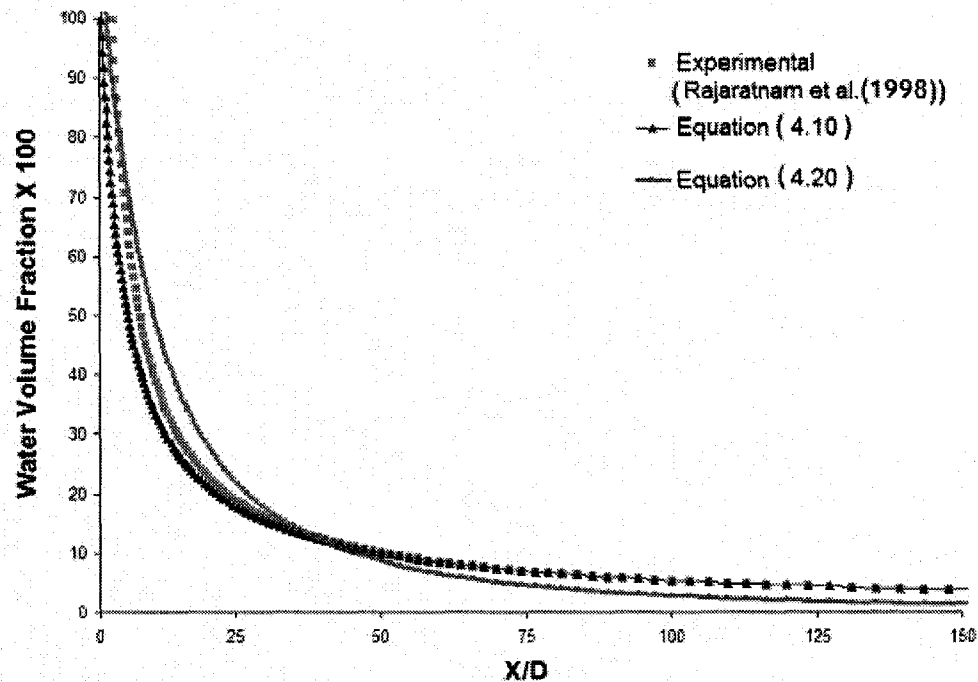
Figure 4.11: Water Phase Volume Fraction along the Jet Centreline According to

Equation (4.10) and Equation (4.20) and Comparison with Experimental

Results of Rajaratnam et al. (1998)

4.7 Conclusion

The polynomial function based empirical mass flux model can accurately predict the volume fraction, velocity and pressure fields of high speed water jets in air. The model predicts the velocity field within $5D$ radial distance from the centreline quite well (Figures 4.5 and 4.6) but in the far field region, the continuum hypothesis (basic assumption of Eulerian multiphase model) becomes invalid and thus the sparse droplet flow (mist zone) is not captured well. An alternative model based on Gaussian distribution (Gaussian distribution based analytical mass flux model) was proposed. This model, although it gives good results, does not seem to be as accurate as the polynomial function based empirical mass flux model. This may be due to inaccurate measurement of the half-width which is needed in this model.

It should be noted that a Lagrangian model is better for simulating sparse droplet flow. From a cleaning application point of view, the mist zone is insignificant. Hence, the model proposed in this study can be very useful in modeling high speed industrial cleaning jets.

Chapter 5

EXPERIMENTAL STUDY OF HIGH SPEED WATER JETS

EMANATING FROM CONVERGING NOZZLES

5.1   Introduction

From the literature review in Chapter 2, we concluded that the experimental works done on high speed water jets are mainly limited to jets emanating from converging-straight nozzles, while converging nozzles are more popular for industrial applications. Also, we pointed out the limitations of the existing works and scope for future experimental research. In this section, an experimental investigation on high speed water jets in air emanating from a converging nozzle is undertaken. The pressure distribution on a target plate for different inlet conditions is studied. Based on experimental results, an empirical pressure distribution model is formulated.

5.2   Experimental Setup

A schematic of the experimental setup is illustrated in Figure 5.1. The capacity of the pump was 100 US-gpm and 750 psi. The converging nozzle used in this study was 45.7 mm long, with largest diameter 14 mm and smallest diameter (D) 7.2 mm. The pressure reducing valve mounted on the line feeding water from the pump to the nozzle was able to reduce the pressure to 150 psi. The static pressure at the nozzle inlet was measured with the aid of a pressure transducer. The flow rate of water through the nozzle was measured using a collecting vessel and stop-watch. The water, flowing out of the

nozzle in the form of a high speed jet, impacted onto a target, which could be moved both axially and radially with the aid of a robotic arm. The target plate had a pressure transducer mounted at its centre. The distance moved by the target in both axial and radial directions was measured by a Linear Variable Displacement Transducer. The signals obtained by the sensors (sampling frequency = 1 KHz) were acquired by a data acquisition system and subsequently analyzed in a computer. Figure 5.2 shows the jet emanating from the nozzle during the experiments.

Experimental Setup

Nozzle Geometry

Inlet Dia =14mm

Exit Dia =7.2mm

Length= 45.7mm
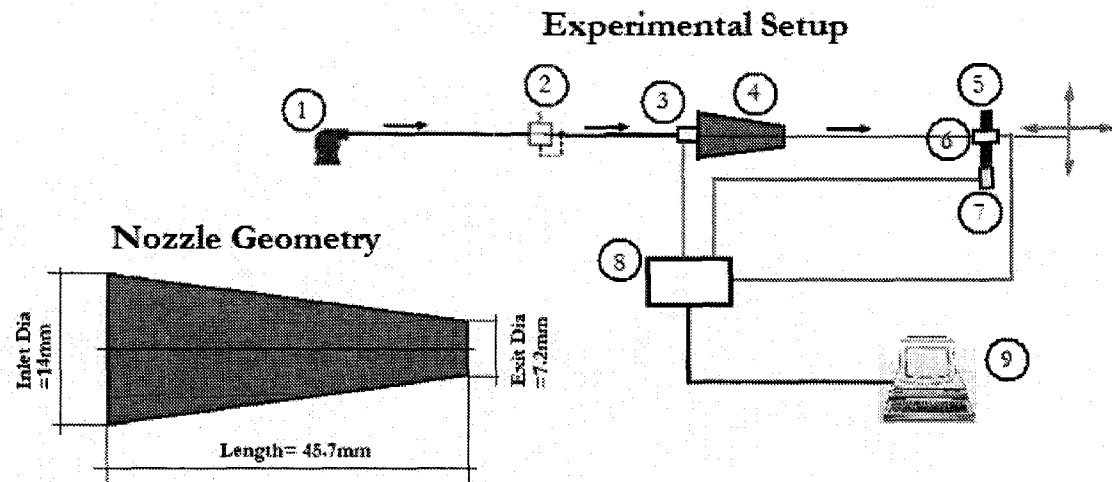
Labels : (1) Pump – 750 psi, 100 US-gpm   (2) Pressure Reducing Valve - up to 150 psi (3) Pressure Transducer – 0 to 1000 psi, 0 to 5 V (4) Converging Nozzle (5) Target Plate (6) Pressure Transducer – 0 to 2000 psi, 0.468 to 10.397 V, 0.005 V/psi (7) Linear Variable Displacement Transducer – ±15 inches, 0-5 V, 1.5 inch/V (8) A/D Converter with 8 channels (9) Computer

Figure 5.1: Schematic of Experimental Setup and Nozzle Geometry

49
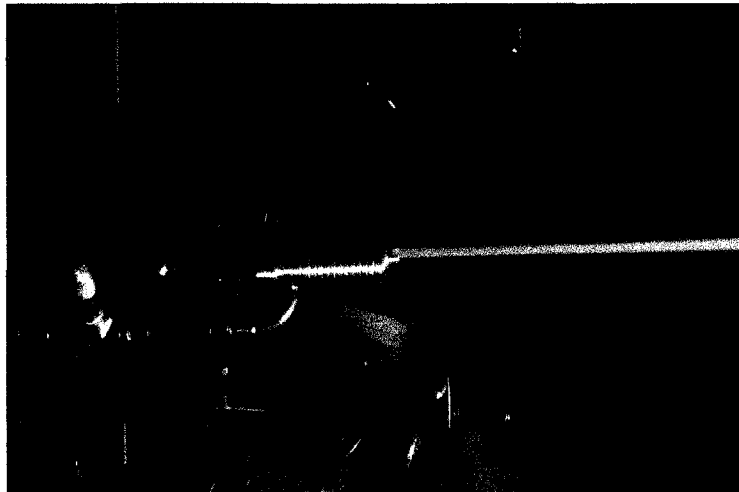
Figure 5.2: High Speed Water Jet Produced in the Experiments

Table 5.1 lists the conditions at the nozzle inlet for which the different test cases of the experiment were performed. Table 5.2 lists the fluid properties at the experimental conditions.

Test Case	Inlet Static Pressure		Inlet Mass Flow Rate	Nozzle Inlet Velocity	Total Pressure at Nozzle Inlet	Nozzle Exit Velocity
	(psi)	(MPa)	(Kg/s)	(m/s)	(MPa)	(m/s)
1	150	1.03	2.217	14.4	1.14	47.8
2	300	2.07	3.096	20.2	2.27	67.4
3	450	3.10	3.796	24.7	3.41	82.6
4	600	4.14	4.274	27.8	4.52	95.1
5	720	4.96	4.613	30.0	5.41	104.0

Table 5.1: Nozzle Inlet and Exit Conditions

50

Properties	Water	Surrounding Air
Density (Kg/m^3)	998.2	1.225
Kinematic Viscosity (m^2/s)	1.0048 x 10^{-6}	1.7894 x 10^{-5}
Specific Heat (J/Kg-K)	4182	1006.43
Thermal Conductivity (W/m-K)	0.6	0.0242
Molecular Weight (Kg/Kg-mol)	18.0152	28.966
Vapor Pressure (N/m^2 (abs))	2.338 x 10^3	N.A.
Temperature (^{o}C)	20	20

Table 5.2: Fluid Properties at Experimental Conditions

5.3 Experimental Procedure

The experiments were run for the test cases 1 to 5. For all the cases, the target plate was moved along the centreline with the aid of a robotic arm from 0.085 m to 0.310 m from the nozzle exit. The starting point was kept at 0.085 m from the nozzle exit in order to ensure that the main stream jet flow does not get obstructed by the rebounding flow from the target plate. The velocity of the robotic arm was 1 cm/sec and thus the relative motion between the jet and the robotic arm was negligible. The target pressure and axial displacement data were recorded during this operation. In this way, the distribution of pressure along the centreline of the jet was obtained. In the next step, test cases 2, 3 and 5 were performed with the target plate kept at a fixed axial distance of 0.3098 m from the nozzle exit and was moved radially. The target pressure and radial displacement data were recorded during this operation. The Spread Coefficients (C) of the jets for different

test cases were obtained with the help of a scale (1 mm resolution) and photographs captured by a Nikon D300 camera.

5.4 Experimental Results

5.4.1 Target Pressure Distribution along the Centreline

Figure 5.3 shows the target pressure distribution along the centreline of the jet for test cases 1 to 4. The target pressure distribution was found to vary linearly with the axial distance. On normalizing the target pressure by total pressure at the inlet and normalizing the axial distance by nozzle exit diameter (D = 0.0072 m), it was found that all the pressure curves collapse onto one curve. Figure 5.4 shows the variation of normalized target pressure with normalized axial distance.
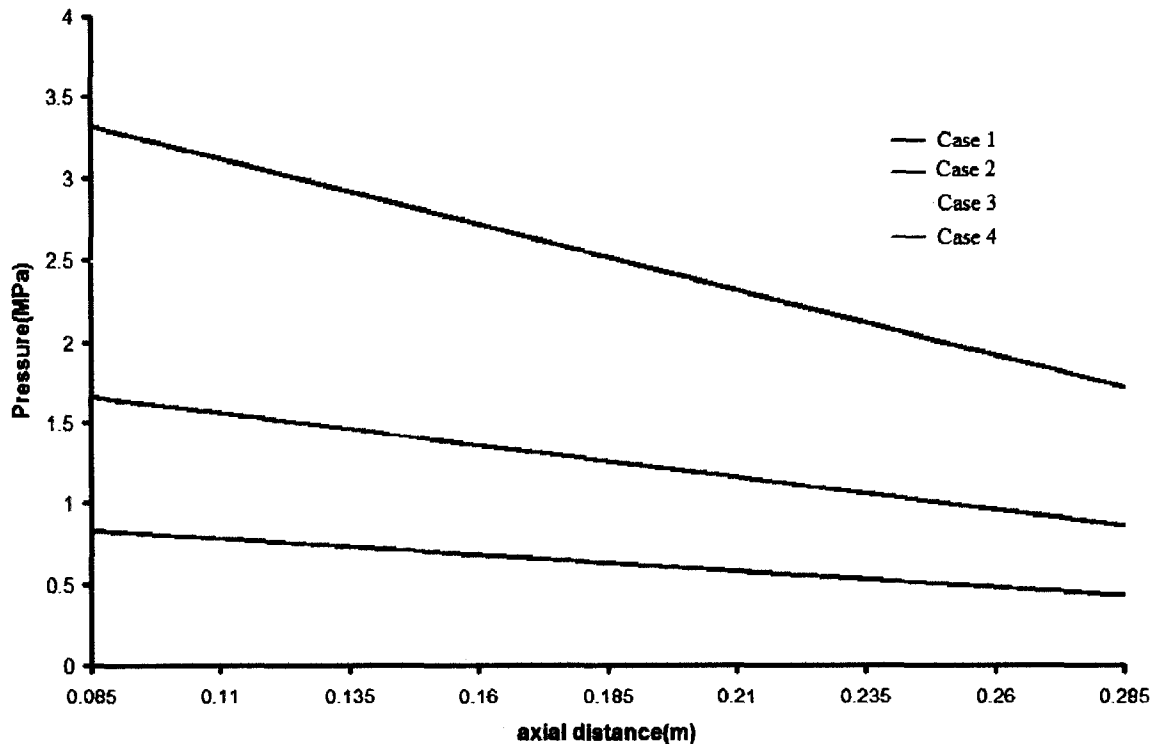
Figure 5.3: Variation of Target Pressure along the Centreline of the Jet

52
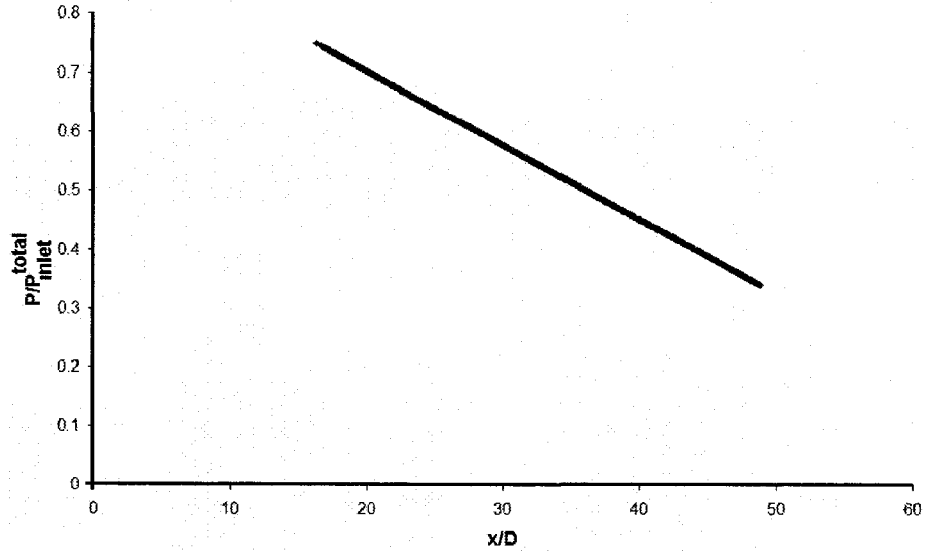
Figure 5.4: Variation of Normalized Target Pressure along the Centreline of the Jet

The equation of the line obtained in Figure 5.4 is

$$\frac{P\left(\frac{x}{D},0\right)}{P_{inlet}^{total}} = -0.0127 \times \left(\frac{x}{D}\right) + 0.9851 \qquad (5.4.1.1)$$

Now, at $x/D = 0$, i.e. at nozzle exit, $P(0,0) = 0.9851\, P_{inlet}^{total}$. Thus the value of 0.9851 is the

ratio of total pressure at the nozzle exit to the total pressure at the nozzle inlet. This value

is slightly less than 1 because some of the pressure is lost in nozzle friction. The linear

decay slope for this nozzle is $m = -0.0127$. Hence Equation (5.4.1.1) can be generalized

as
$$\frac{P\left(\frac{x}{D},0\right)}{P_{inlet}^{total}} = m \times \left(\frac{x}{D}\right) + \frac{P_{exit}^{total}}{P_{inlet}^{total}} \qquad (5.4.1.2)$$

As has been already mentioned, the pressure measurement along the centreline was

started from a distance of 0.085 m from the nozzle exit. This is because it is extremely

difficult to measure pressure accurately near the nozzle exit as the jet flow rebounds after

hitting the target and interferes with the main flow. Thus equations (5.4.1.1) and (5.4.1.2) are based on the assumption that this linear curve will be maintained up to the nozzle exit.

5.4.2 Target Pressure Distribution in Radial Direction

In this experiment, the test cases 2, 3 and 5 were performed with the target plate located at a fixed axial distance of 0.3098 m from the nozzle exit and was moved radially. Figure 5.5 shows the radial distribution of target pressure for all the three cases, while Figure 5.6 shows the same distribution after normalizing the pressure by the corresponding pressure on the jet axis and radial distance by nozzle exit diameter.
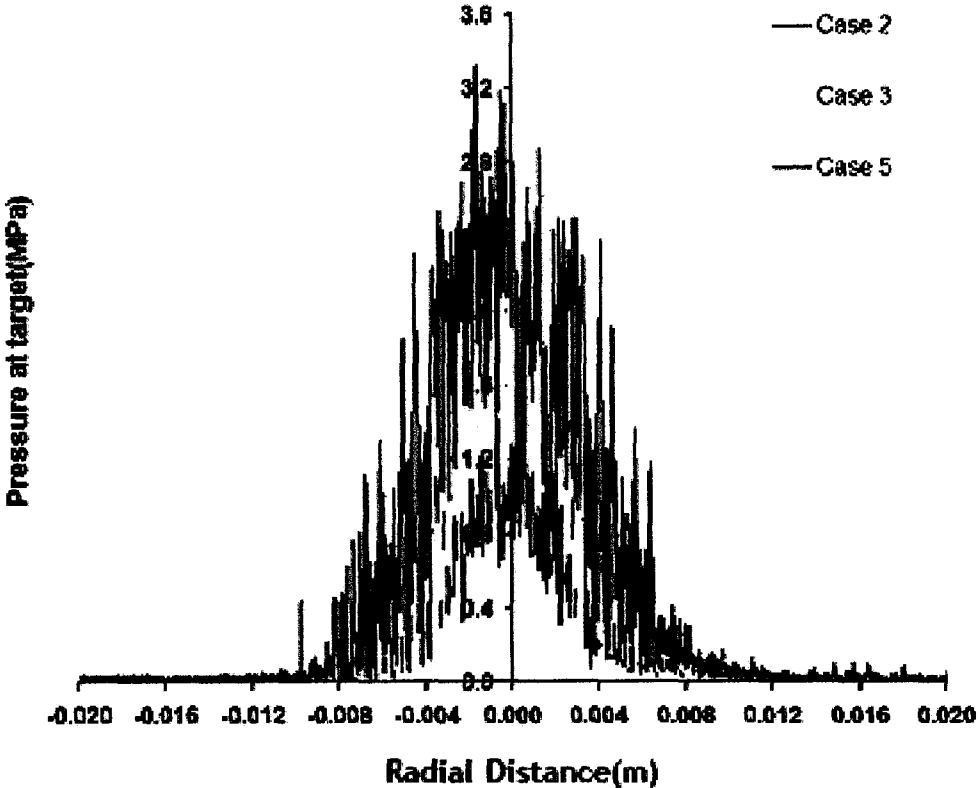
Figure 5.5: Variation of Target Pressure along the Radial Direction
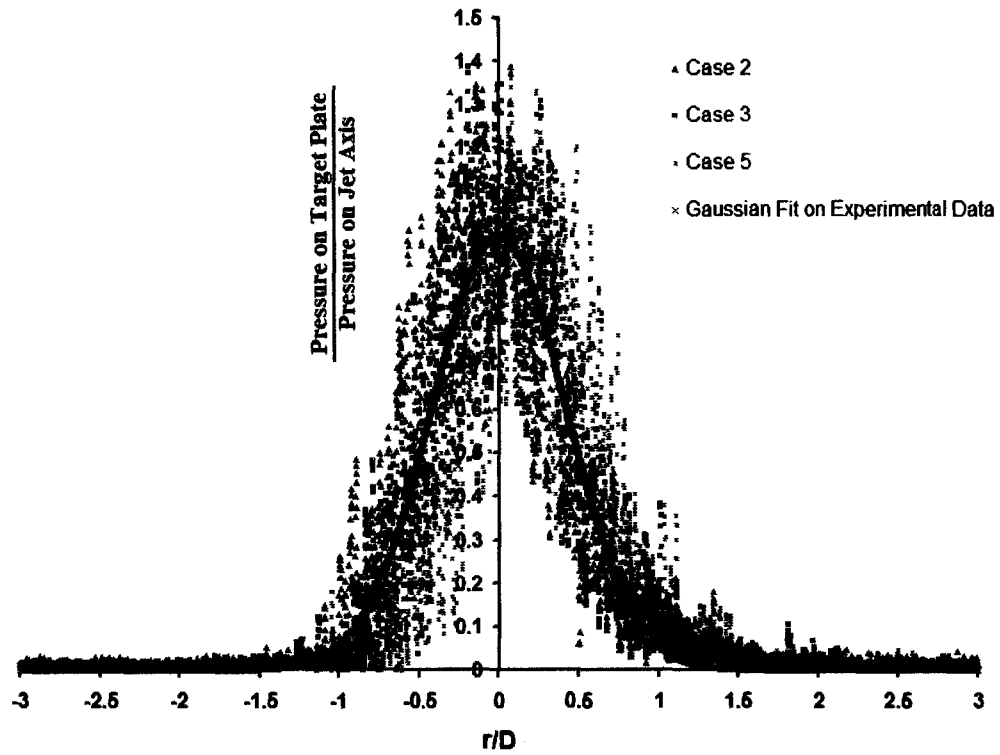
Figure 5.6: Variation of Normalized Target Pressure along the Radial Direction

Examining Figure 5.6, it appears that all the curves collapse into a single curve and the distribution closely resembles a Gaussian distribution. The equation of the Gaussian curve fit on the normalized pressure distribution is

$$\frac{P\left(\frac{x}{D}, \frac{r}{D}\right)}{P\left(\frac{x}{D}, 0\right)} = \exp\left(-2.8345\left(\frac{r}{D}\right)^2\right) \tag{5.4.2.1}$$

The radial position (R_{Patm}) corresponding to the value zero of the Gaussian curve fit is the position where the pressure on the target plate is equal to the atmospheric pressure. The value of R_{Patm} is found to be $1.68D$.

55

5.4.3 Estimation of the Spread Coefficient

Spread coefficient (C) is the growth rate of the width of the outer region of a jet. To measure it, a scale was located at a fixed axial location from the nozzle exit and was perpendicular to the jet axis. Digital photographs of the jet and the scale were taken with a Nikon D300 Camera and the width of the jet at that particular axial location was determined. The process was repeated for different axial locations of the scale and finally, the average of the measured values of the Spread Coefficient was taken. The whole process was performed for different experimental test cases. The mathematical formulation of estimation of Spread Coefficient is

$$C = \frac{\text{Radial width of the jet at the location of the scale - Nozzle Exit Radius}}{\text{Axial distance between the scale and the nozzle exit}} \quad (5.4.3)$$

Table 5.3 shows the value of the Spread Coefficients corresponding to different test cases.

Test Case	Spread Coefficient (C)
1	0.012
2	0.028
3	0.037
4	0.043
5	0.056

Table 5.3: Spread Coefficients

5.5 Analysis of Experimental Results

From the experimental results, we have determined the pressure distribution on the target plate. The pressure is maximum at the centreline and its distribution is Gaussian in

the radial direction. The distribution of target pressure along the centreline is found to vary linearly. As the jet progresses, it transfers momentum to the surroundings and thus continues to spread. This results in not only a reduced peak pressure at the target plate, but also a decrease in overall pressure distribution. Figure 5.7 illustrates this phenomenon.
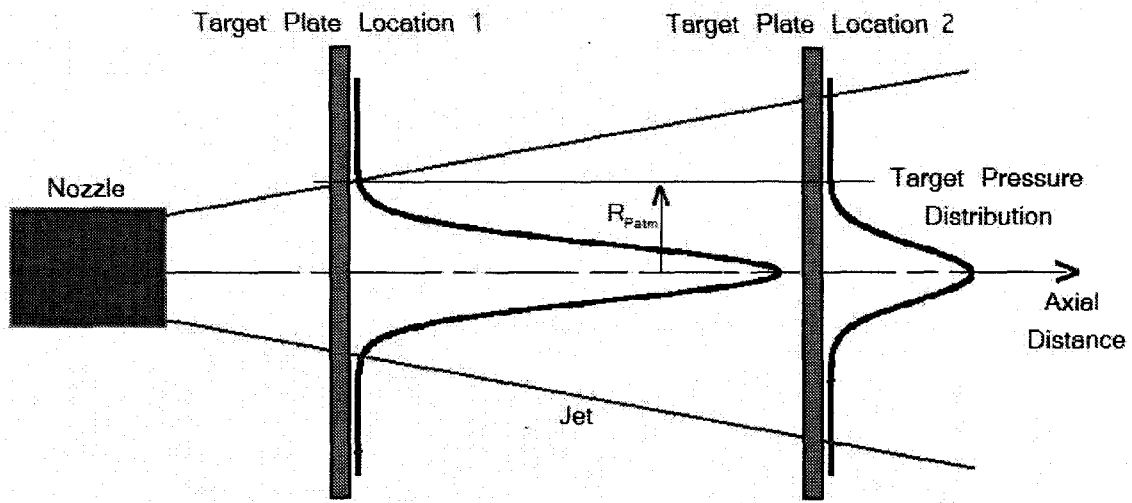
Figure 5.7: Pressure Distribution on the Target Plate

Combining Equations (5.4.1.2) and (5.4.2.1), we obtain

$$P\left(\frac{x}{D}, \frac{r}{D}\right) = P_{inlet}^{total}\left[m \times \left(\frac{x}{D}\right) + \frac{P_{exit}^{total}}{P_{inlet}^{total}}\right] \times \exp\left(-2.8345\left(\frac{r}{D}\right)^2\right) \qquad (5.5.1)$$

Equation (5.5.1) is the generalized equation of target pressure distribution. From Figure 2.3 we observe that Leach et al. (1966) showed that the decay of target pressure along the centreline is linear at axial distances near the nozzle, but non-linearity increases

at distances far away. The slopes (m) of the linear region of the target pressure decay curves are different for different nozzle geometries. Thus, equation (5.5.1) will be valid for different nozzles for axial distances not too far downstream from the nozzle exit.

It is interesting to note that this value of R_{Patm} (radial width at which the target pressure is equal to the atmospheric pressure) is invariant with the axial position of the target plate. Examining Equation (5.5.1) we observe that the exponential part which represents the distribution of the pressure on the target plate is only dependent upon the radial coordinate. Thus, although the jet spreads in air and its radial width increases, the radial location where the target pressure turns atmospheric (R_{Patm}) remains fixed at the value of $1.68D$ (See Figure 5.7). This observation is in congruence to that of Leach et al. (1966).

5.6 Comparison with Previous Work

Leach et al. (1966) studied the target pressure distribution in the direction perpendicular to the jet flow at two different axial distances, $76D$ and $330D$ (Figure 2.4) and analytically obtained the radial pressure distribution (Equation (2.2)) which fit well to their experimental data. From their study, it is obvious that nozzle geometry can significantly affect the jet characteristics. They found that although the decay of centreline target pressure varies for different nozzle geometries (converging-straight nozzles give least decay), the target pressure distribution normalized by the corresponding pressure on the jet axis is similar not only for different nozzle geometries but also for different inlet pressures. This has also been corroborated by our experimental results (Figure 5.6). We found from our experimental results that the point where the

pressure at target plate is equal to the atmospheric pressure is $1.68D$ while the results of

Leach et al. (1966) predict a value around $1.3D$. The difference may occur due to the fact

that their prediction is based on an analytical curve which is a third order polynomial

satisfying the boundary conditions of the given problem. Our results are based on

Gaussian curves fitted on the experimental data, and these curves fit have R-squared

value ~ 0.97. Also, their nozzle geometry and inlet conditions were different from ours,

which might have some small effect in this regard. Figure 5.8 shows the comparison

between our experimental results and the analytical curve obtained by Leach et al.

(1966).
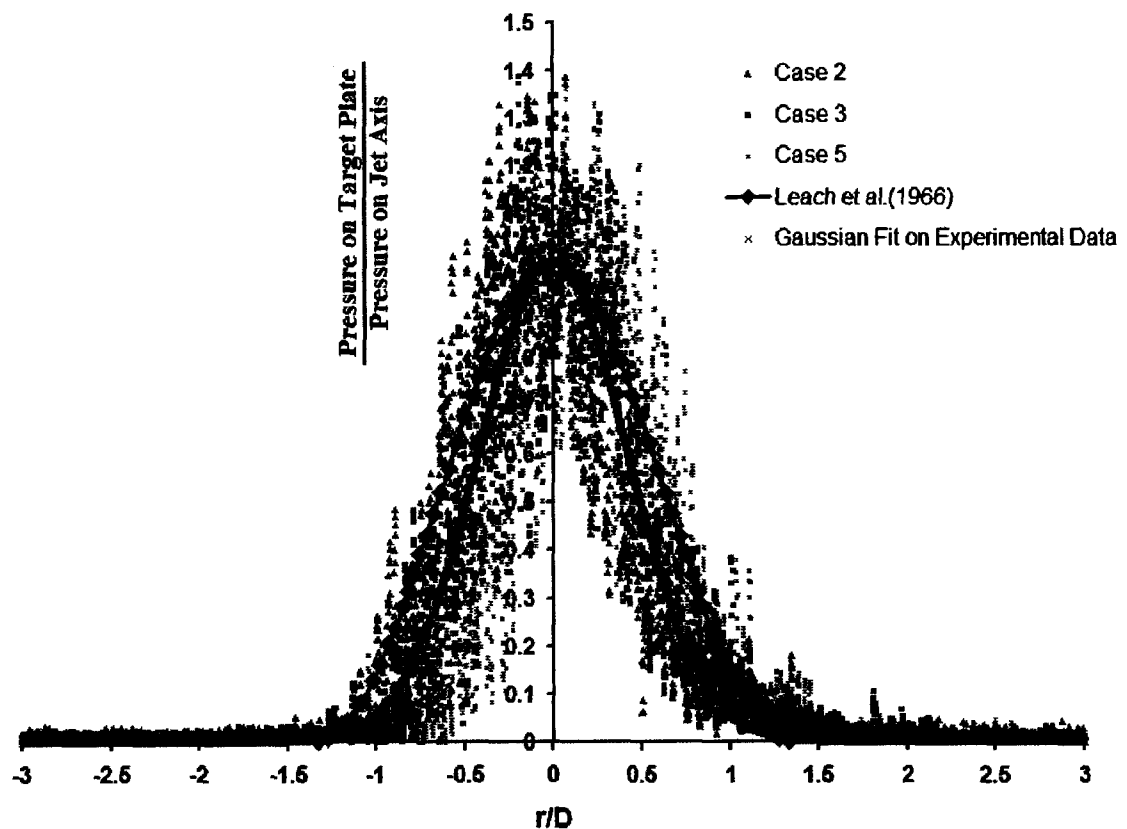
Figure 5.8: Normalized Target Pressure along the Radial Direction and Validation

with Leach et al. (1966)

59

The figure shows that the curve fit of Leach et al. (1966) is slightly towards the outer limit of our experimental results. Also their curve under-predicts the pressure decay near the edge of the jet. The Gaussian fit gives a very good prediction of the entire phenomenon.

Unlike Leach et al. (1966), our focus was on regions close enough to the nozzles (axial distances within $45D$) because this region has significant momentum to deliver to the target plate (cleaning surface). Leach et al. (1966) obtained the decay of pressure along the centreline for different nozzle geometries and studied up to axial distances of $700D$. Their curves (Figure 2.3) show that the decay is non-linear for long axial distances while almost linear in the regions near the nozzle. Analyzing their experimental data, we found that the magnitude of the slope of target pressure decay along the centreline is 0.0018 (for converging straight nozzle, see Figure 2.2a), while for our converging nozzle, the slope is 0.0127. Thus, one can conclude that converging-straight nozzles are more effective in delivering pressure to the target plate than converging nozzles.

Chapter 6

NUMERICAL STUDY OF HIGH SPEED WATER JETS

EMANATING FROM CONVERGING NOZZLES

6.1 Introduction

In Chapter 3, we derived the polynomial function based empirical mass flux model and validated it against the experimental works of Rajaratnam et al.(1994,1998) and Leach et al.(1966). In this Chapter, we validate the model with our experimental results discussed in Chapter 5.

6.2 Computational Domains and Solver Parameters

The computational domain was created in GAMBIT and was divided into two regions, (a) the nozzle region and (b) the jet region.

6.2.1 Nozzle Region

Since the nozzle is axisymmetric, only half of the domain was simulated in a two dimensional axisymmetric space, as illustrated in Figure 6.1. The geometry of the nozzle has been discussed in section 5.2 and in Figure 5.1. The axial length of the cells at the inlet was 2 mm and gradually decreased along the axis with a successive ratio of 0.98. The grid was clustered near the nozzle exit to enable us to capture the flow gradients with considerable accuracy. The radial width of the cells was 0.39 mm, except near the wall

boundary where it has been reduced to 0.2 mm to capture the gradients due to the boundary layer.
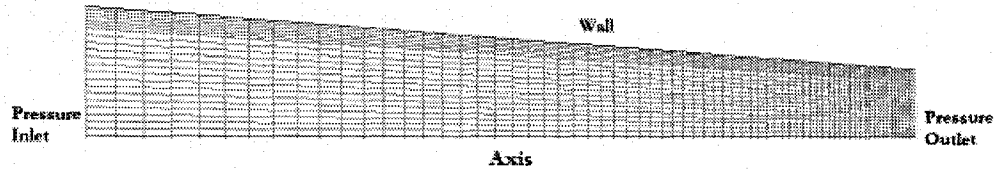
Figure 6.1: Nozzle Geometry, Boundary Conditions and Meshing

The nozzle inlet had pressure inlet conditions (equal to the nozzle inlet pressure for the particular case considered, as outlined in Table 5.1) while a pressure outlet condition (equal to the atmospheric pressure) is applied at the nozzle exit. FLUENT was used as the flow solver. Since the nozzle is completely filled with water, the single phase Eulerian model is employed. Pressure-velocity coupling was achieved through the SIMPLE algorithm. The standard k-ε turbulence model was used and turbulence intensity of 10% was assumed at the nozzle inlet. A steady state computation of the nozzle flow was performed and, when the residuals were low enough ($\sim 10^{-6}$), the profiles of the flow parameters at the nozzle exit were used as the input (inlet) to the adjacent computational domain, i.e., the jet region. The default under-relaxation parameters of FLUENT were used in the computation. The discretization schemes used in this simulation are listed in Table 6.1.

Variables	Discretization Scheme
Momentum	QUICK
Volume Fraction	QUICK
Turbulent Kinetic Energy	Second Order Upwind
Turbulent Dissipation Rate	Second Order Upwind

Table 6.1: Discretization Schemes for Nozzle Flow

6.2.2 Jet Region

Since the emanating jet is circular, only half of the domain was simulated in a two

dimensional axisymmetric space, as shown in Figure 6.2.
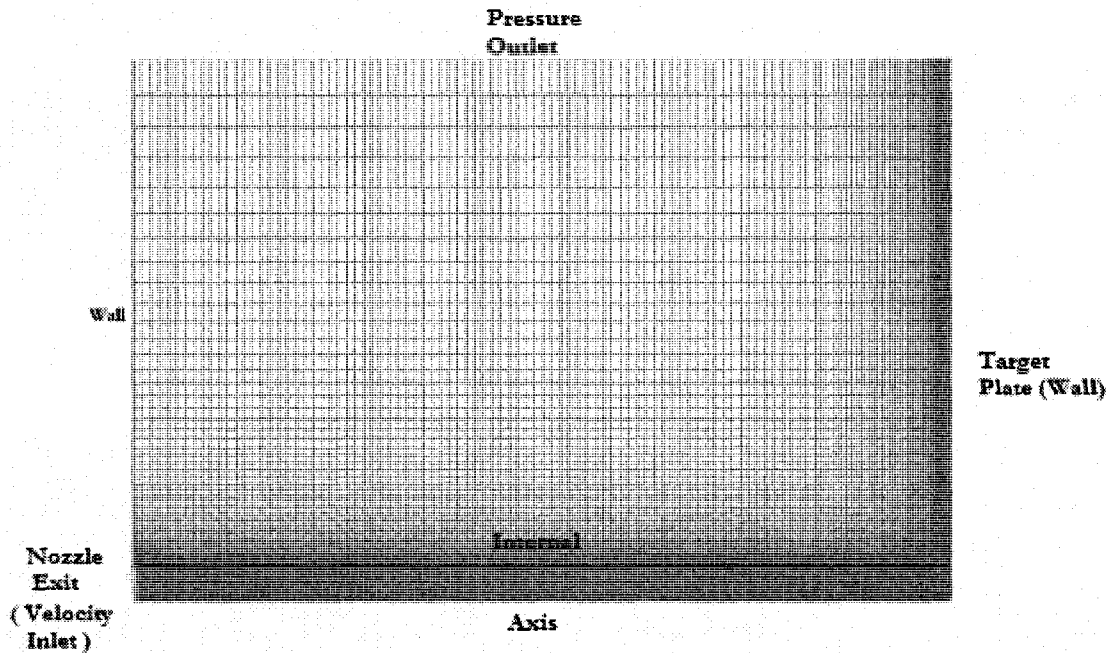
Figure 6.2: Boundary Conditions and Meshing in Jet Region

The axial length of the cells at the inlet was 1.5 mm and gradually decreased along the

axis with a successive ratio of 0.95. Grid clustering near the target plate was incorporated

to accurately capture the high gradients at the target plate. The domain was divided into

two parts by introducing an internal boundary condition, enabling us to have different

mesh distributions in the two parts. The part near the axis was formed with cells of

uniform radial width of 0.2 mm. This small spacing was essential to capture the mass

transfer accurately. In the other region, the largest radial cell width was 1.5 mm, located at the pressure outlet boundary. There was a gradual decrease in the radial width of the cells by a successive ratio of 0.93. This provided a very fine grid ($\sim$ 0.1 - 0.2 mm) in the region where jet-air interface was expected. The nozzle exit velocity and turbulence profiles obtained by solving the nozzle flow were applied as inlet conditions (velocity inlet). Since we intend to simulate the Case (a) (test cases 2, 3 and 5) referred in Chapter 5, the length of the domain was set at 0.3098 m while the width of the domain was 152.4 mm. The domain was wide enough to ensure that the pressure outlet boundary condition (set at atmospheric pressure) does not adversely affect the flow field.

FLUENT was used as the flow solver. The Eulerian multiphase model and standard k-ε turbulence model with standard wall functions were used to capture the flow physics. Water was treated as the secondary phase. The drag coefficient between the phases was determined by the Schiller-Naumann equation (see Chapter 3). The polynomial function based empirical mass flux model was incorporated into the continuity and momentum equations in the same way as referred in Chapter 4. Pressure-velocity coupling was achieved using the phase-coupled SIMPLE algorithm. All the residuals were set to 10^{-6} and the time step size was 10^{-5} seconds. The program was run for a time which was long enough to attain quasi-steady state. The default under-relaxation parameters of FLUENT were used in the computation. The discretization schemes used in the simulation are listed in Table 6.2.

Variables	Discretization Scheme
Time	First Order Implicit
Momentum	QUICK
Volume Fraction	QUICK
Turbulent Kinetic Energy	Second Order Upwind
Turbulent Dissipation Rate	Second Order Upwind

Table 6.2: Discretization Schemes for Jet Flow

6.3 Sample Simulation Result of the Nozzle Flow

Figures 6.3 and 6.4 show the velocity and turbulence intensity contours obtained by numerically simulating the nozzle region corresponding to Test Case 3 (see Chapter 5).
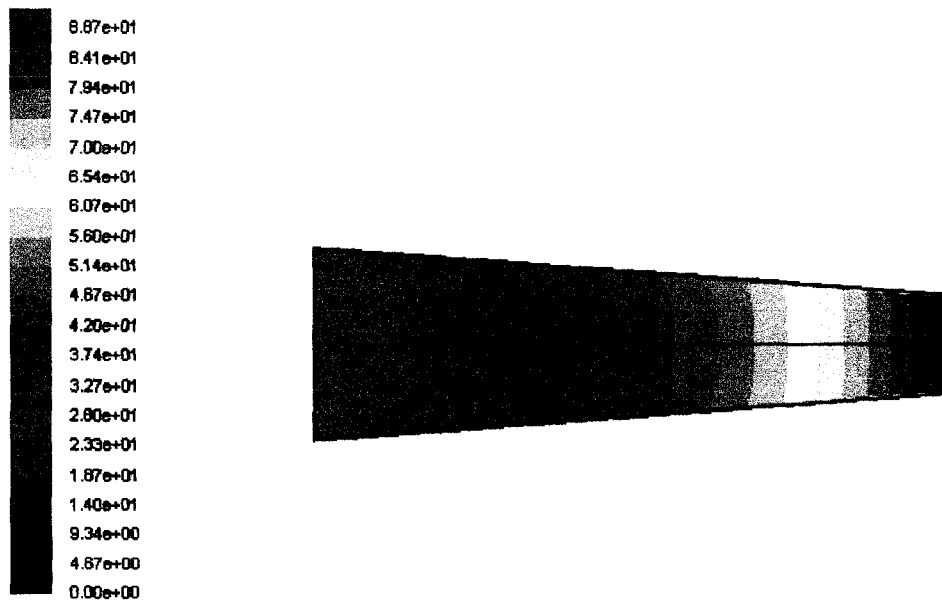
Figure 6.3: Velocity Distribution Inside the Nozzle

2.29e+01
2.21e+01
2.14e+01
2.07e+01
1.99e+01
1.92e+01
1.85e+01
1.77e+01
1.70e+01
1.63e+01
1.55e+01
1.48e+01
1.41e+01
1.33e+01
1.26e+01
1.18e+01
1.11e+01
1.04e+01
9.63e+00
8.90e+00
8.16e+00

Figure 6.4: Turbulence Intensity Inside the Nozzle

The profiles of these quantities at the nozzle exit were used as the inlet conditions in the jet flow region. Similar simulations were performed for the other test cases as well.

6.4 Simulation Results of the Pressure Distribution at the Target Plate

Recalling Section 5.4.2, three experimental test cases, viz. Test Cases 2, 3 and 5 (refer to Table 5.1) were considered with the target plate placed at an axial distance of 0.3098 m from the nozzle exit. Analysis of the experimental results have shown that the normalized pressure distribution on the target plate for all these three cases collapse into one curve which can be represented by a Gaussian distribution (see Figures 5.6, 5.8 and Equation (5.4.2.1)). Corresponding to each of the test cases, simulations were performed and are referred to as SIM-2, SIM-3 and SIM-5.

Simulation Test Case	Experimental Test Case	Total Pressure at Nozzle Inlet (MPa)	Spread Coefficient	Mean Velocity at Nozzle Exit (m/s)	Axial Distance of Target Plate from Nozzle Exit	
					(m)	x/D
SIM-2	2	2.27	0.028	67.4	0.3098	43.03
SIM-3	3	3.41	0.037	82.6	0.3098	43.03
SIM-5	5	5.41	0.056	104.0	0.3098	43.03

Table 6.3: Simulation Conditions

The pressure distribution on the target plate obtained by a Gaussian curve fit of the experimental data (see Equation (5.5.1)) is written as:

$$P\left(\frac{x}{D}, \frac{r}{D}\right) = P_{inlet}^{total}\left[m \times \left(\frac{x}{D}\right) + \frac{P_{exit}^{total}}{P_{inlet}^{total}}\right] \exp\left(-2.8345 \left(\frac{r}{D}\right)^2\right) \tag{6.1}$$

where m=-0.0127 and $\dfrac{P_{exit}^{total}}{P_{inlet}^{total}}$=0.9851 .

Hence, corresponding to each of the experimental test cases, the term P_{inlet}^{total} (See Table 5.1) will vary and thus different distributions of pressure on the target plate will be obtained. Each of these Gaussian distributions will be compared with the corresponding results obtained from the numerical simulations. The values of the Spread Coefficients used as an input to the mass-flux model were obtained from Table 5.3.
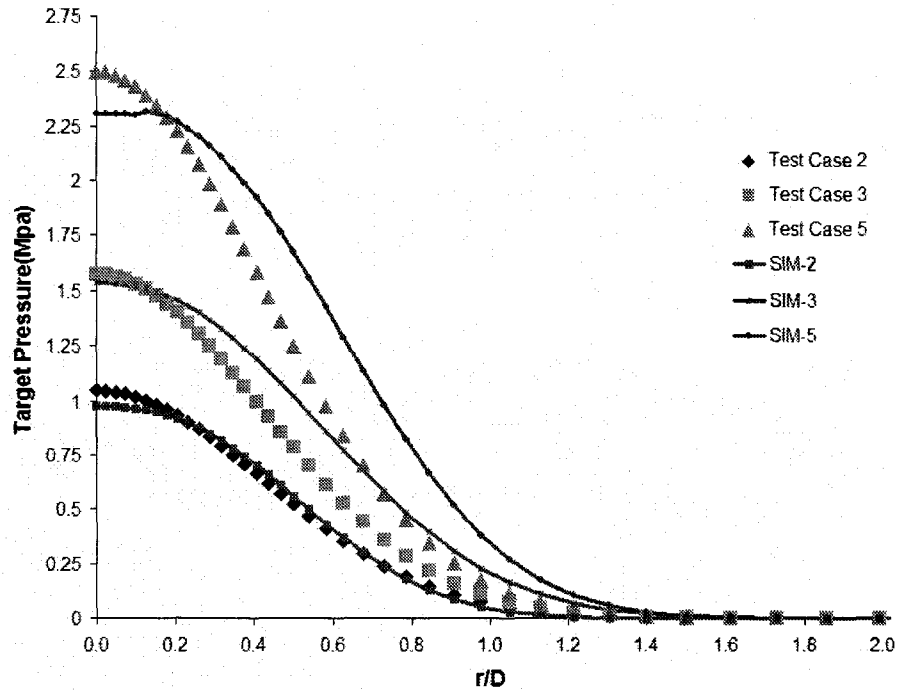
Figure 6.5: Comparison of Simulation and Corresponding Experimental Results for

Target Pressure

Figure 6.5 shows the comparison between the experimental test cases and their corresponding numerical simulations. It can be observed that the simulation results predict the experimental data with considerable accuracy. The distributions obtained in the simulations slightly over-predict the experimental data while the target pressure at the centreline is a bit under-predicted. This might be because of the fact that the Spread Coefficients, given as an input to the mass-flux model, were not measured very precisely.

6.5 Velocity and Volume Fraction Distributions

We are also interested in analyzing the velocity and volume fraction distributions for each of the simulation cases. Figures 6.6 and 6.7 show the velocity and volume

fraction contours for the case SIM-2. From these figures, it is evident that these jets have much less spread compared to the case discussed in Chapter 4.
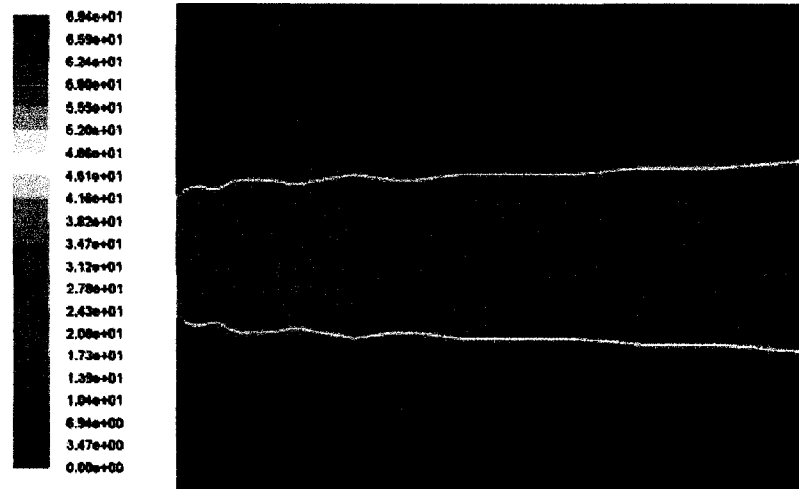
Figure 6.6: Contour of Water Phase Velocity in the Jet (within x/D=5)
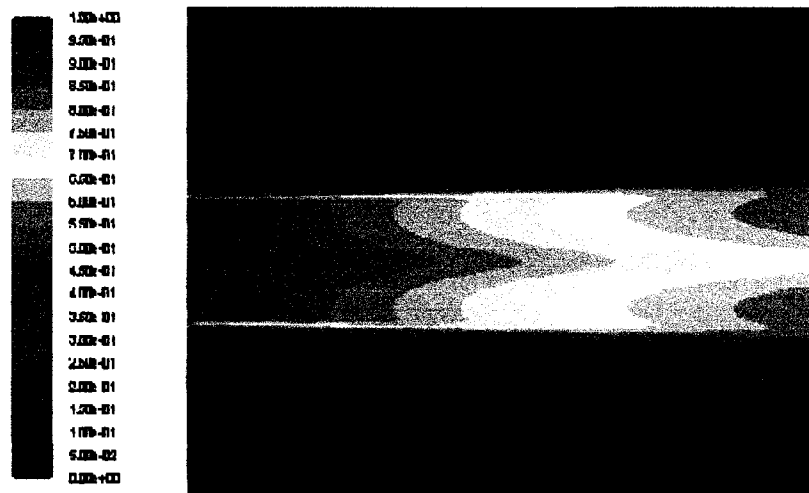
Figure 6.7: Contour of Water Phase Volume Fraction in the Jet (within x/D=5)

Corresponding to each of the simulation cases, the velocity and volume fraction distributions in the radial direction were obtained for axial positions x/D = 10, 20 and 30.

6.5.1 SIM-2
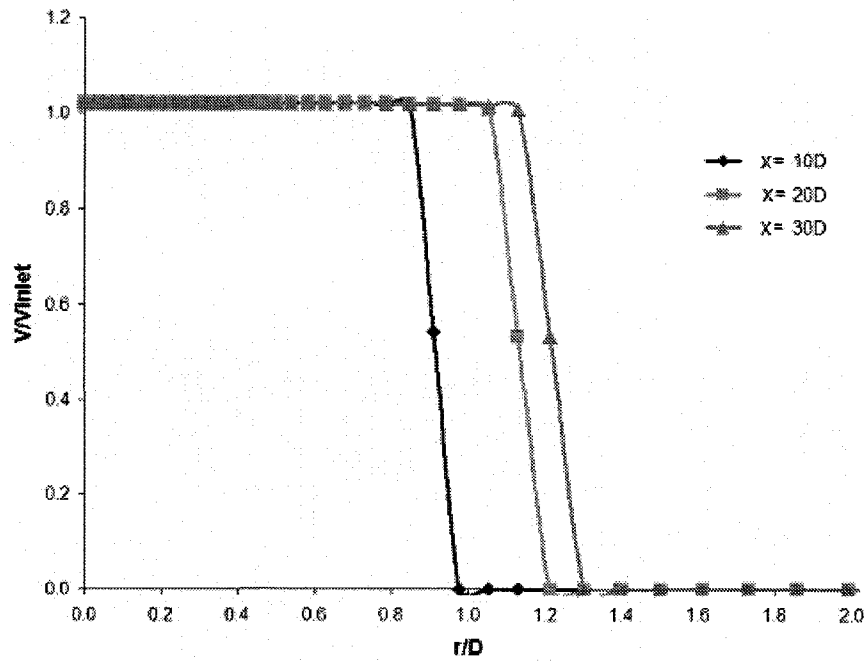
Figure 6.8: Normalized Velocity versus Normalized Radial Distance
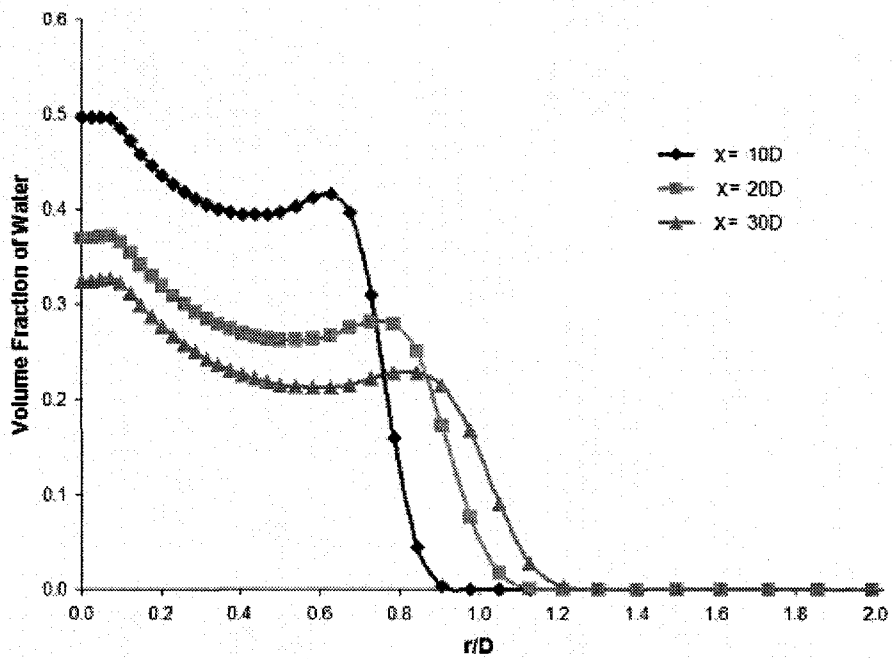
Figure 6.9: Volume Fraction versus Normalized Radial Distance

6.5.2 SIM-3
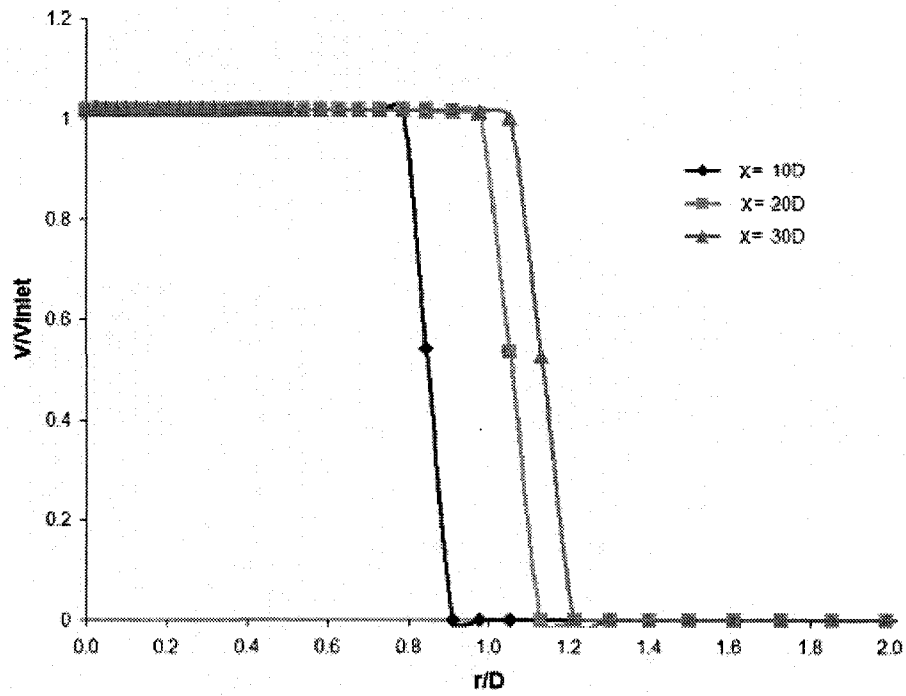
Figure 6.10: Normalized Velocity versus Normalized Radial Distance
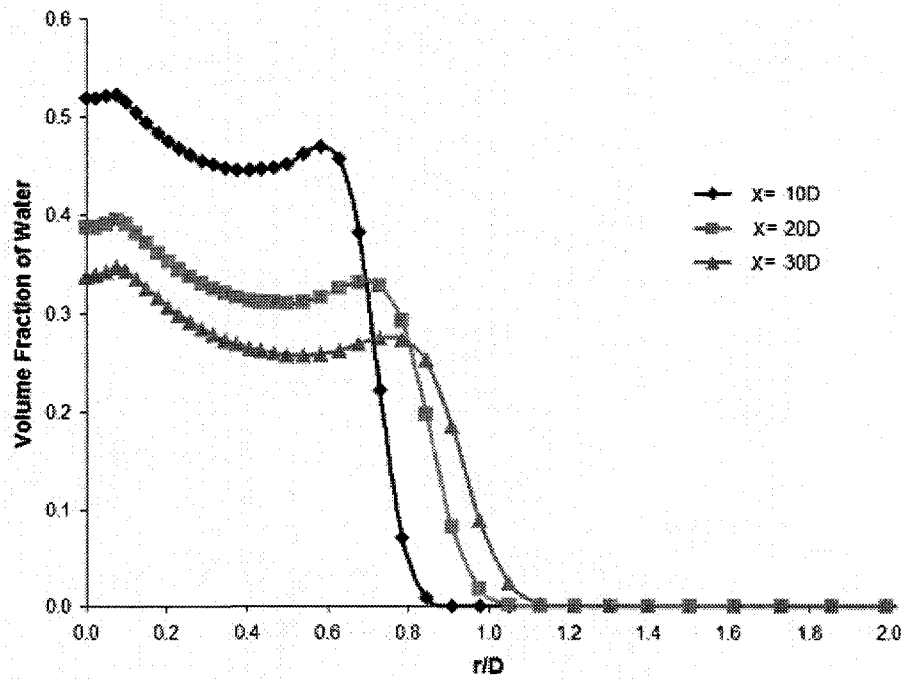
Figure 6.11: Volume Fraction versus Normalized Radial Distance

6.5.3 SIM-5

Figure 6.12: Normalized Velocity versus Normalized Radial Distance
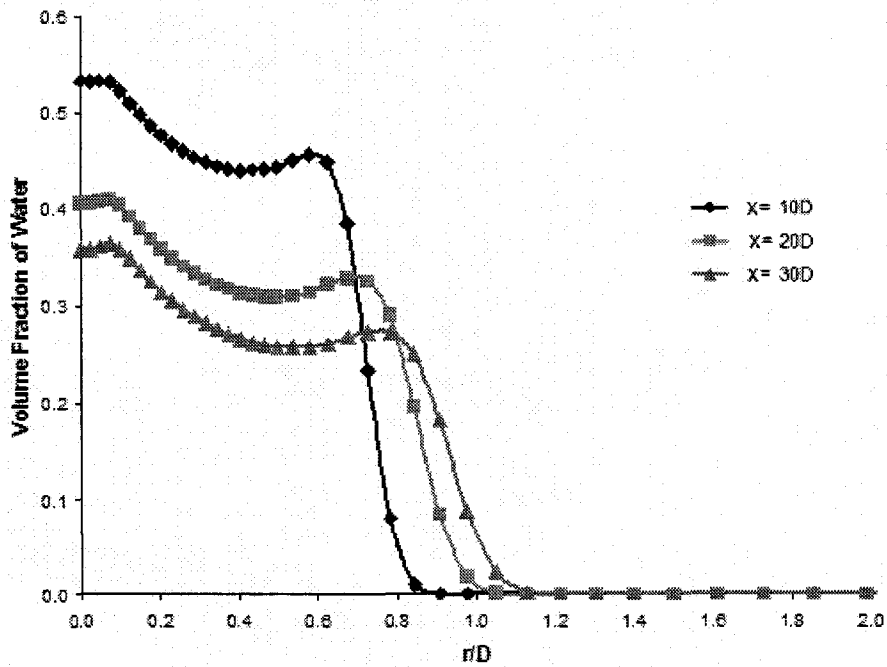
Figure 6.13: Volume Fraction versus Normalized Radial Distance

6.6 Analysis of Velocity, Pressure and Volume Fraction Distributions

In all the simulation cases, the velocity profile is top-hat even at x/D = 30, which implies the existence of potential core. In Figure 6.5, the flatness of pressure curves near the centreline also suggests the existence of potential core when the jet hits the target plate (kept at x/D = 43.03). During the experiments, the pressure transducer used to measure the pressure at th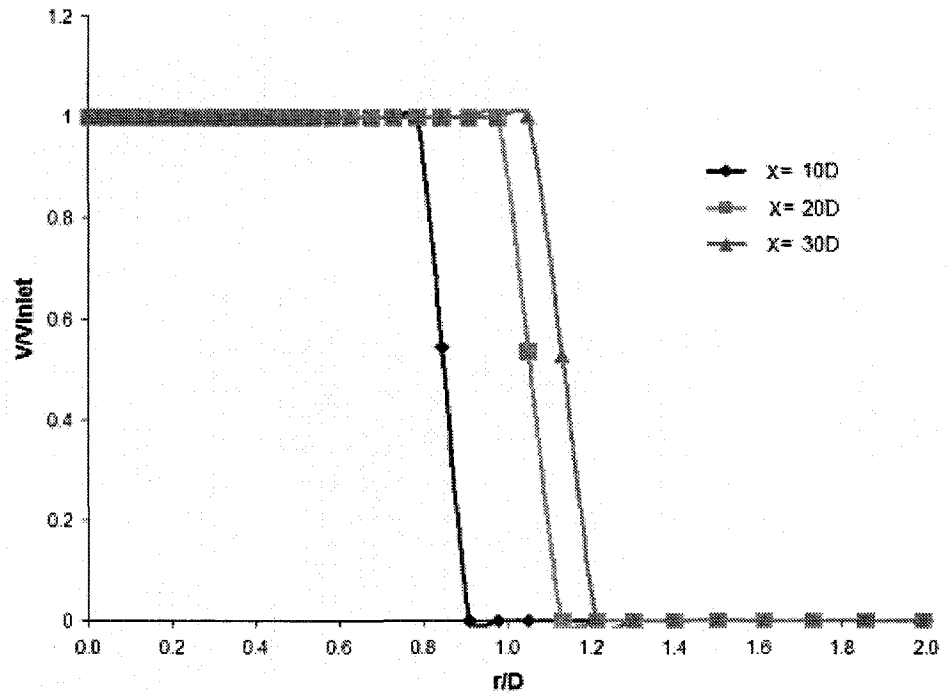e target plate was of 9 mm diameter. This large size of the transducer may be the reason behind the failure to capture the effect of the potential core at the target plate. Also, the Gaussian fit, having the R-squared value ~0.97 may not be the best fit and a distribution close to Gaussian with a flatter top might be more suitable in this case. The distributions obtained in the simulations slightly over-predict the experimental data while the target pressure at the centreline is a bit under-predicted. This might be because of the fact that the Spread Coefficients, given as an input to the mass-flux model, were not measured very precisely.

Although the velocity distribution is very flat, the volume fraction distribution shows a kind of Gaussian profile with a bulge. Since the mist region was not included in the numerical modeling, the volume fraction of water actually lost as mist numerically accumulates near the jet-air interface and produces the erroneous bulging effect. The bulging effect flattens out with increased axial distance. It is seen that the volume fraction decreases rapidly with increased axial distance while the velocity remains fairly constant. Also the volume fraction profile is thinner than the velocity profile. These phenomena have already been reported by Rajaratnam et al. (1998) and numerically verified in Chapter 4.

Chapter 7

CONCLUSIONS AND RECOMMENDATIONS

7.1 Conclusions

A novel numerical model was built to capture the flow physics of high speed water jets in air. The model was validated against published experimental works. Experimental investigations on pressure distribution on a target plate placed in the jet flow field were performed. An empirical equation for the pressure distribution on the target plate was formulated. The results obtained from the numerical model were compared with the experimental results. Both experimentally and numerically, the physics of high speed jet flow was analyzed. The salient observations can be summarized as follows:

- The Equation for pressure distribution on a target plate is given by

$$P\left(\frac{x}{D}, \frac{r}{D}\right) = P_{inlet}^{total}\left[m \times \left(\frac{x}{D}\right) + \frac{P_{exit}^{total}}{P_{inlet}^{total}}\right] \exp\left(-2.8345\left(\frac{r}{D}\right)^2\right)$$

This equation is valid when the target plate is placed close enough ($< 50D$) from the nozzle exit. It was found that the normalized target pressure along the centreline varies linearly with axial distance and the curves are similar for different inlet pressures. After $\sim 100D$, the amplitude part of this distribution will vary non-linearly with axial distance. The exponential part is invariant not only for different inlet pressures but also for different nozzle geometries. The radial width along the target plate where the target

pressure becomes equal to the atmospheric pressure was found to be $1.68D$ and this width is also invariant.

- The polynomial function based empirical mass flux model relates the mass flux of water phase in the jet to the mass flux at the nozzle exit. The equation is given by

$$\dot{M}(x,r) = \frac{5.62 \dot{M}_0 R_0{}^2}{R^2} \left\{ 1 - \left(\frac{r}{R} \right)^{1.5} \right\}^3$$

- The Gaussian distribution based analytical mass flux model is another method of relating the mass flux of water phase in the jet to the mass flux at the nozzle exit. The equation is given by

$$\dot{M}\left(x,\frac{r}{b_w}\right) = \dot{M}_0 \, 0.693 \left(\frac{R_0}{b_w} \right)^2 \left[1 - \exp\left(-0.693 \left(\frac{R}{b_w} \right)^2 \right) \right]^{-1} \exp\left(-0.693 \left(\frac{r}{b_w} \right)^2 \right)$$

- The simulation results show that even at the location $x/D = 30$, the normalized (w.r.t inlet velocity) radial distribution of velocity is top hat with a value of 1. But we can observe that the water volume fraction distribution falls almost like a Gaussian curve, with centreline value ~0.35. Thus we can conclude that there is a lot of air entrained within the potential core (of uniform velocity).

7.2   Contributions

Although there has been significant development in the numerical modeling of high speed sprays by using models based on statistical techniques, yet, to the best of our

knowledge, our approach is the first step in numerical modeling of high speed jet flows. The polynomial function based empirical mass flux model proposed in this work predicts the flow physics of high speed jet flows quite accurately, specially in the near-field region. The model is mainly dependent on parameters like the mass-flux at the nozzle exit and the spread coefficient of the jet. These parameters can be obtained experimentally without much difficulty. Since particle tracking methods or extra transport equations are not involved in this model, the computational cost is not an issue.

Also an experimental work was performed in this research. An empirical equation for the pressure distribution at the target plate placed at a given axial location in the jet flow field was formulated.

7.3 Recommendations

The polynomial function based empirical mass flux model can be extended to incorporate the effect of nozzle. Right now, the Spread Coefficient of the jet is determined from digital photographs taken by Nikon D300 camera. It was extremely difficult to capture the interface between the main region and the mist region of the jet, thus there were manual errors in determining the Spread Coefficients. More sophisticated digital cameras can be used to reduce the possibility of manual errors .It is to be noted that the value of Spread Coefficient is dependent on several nozzle parameters like nozzle geometry, velocity, turbulence, cavitation, etc as well as ambient condition like aerodynamic effects. There is a need to develop numerical models that can combine the

nozzle flow characteristics with the emanating jet. By this process, the jet spread can be determined numerically without any experimental intervention.

There is a need to incorporate the effect of turbulence in the polynomial function based empirical mass flux model. Since the turbulence transport phenomena for high speed water jets in air is not well known to us, no extra term was incorporated into the transport equations for turbulence quantities. Our numerical simulations were performed with Standard k-ε turbulence model. Other advanced turbulence models like RNG k-ε or LES can affect the results and there is a need to analyze the effect of those models. Also, to build a complete mass-flux model, there is a need to incorporate the effect of the mist region of the jet which is not properly handled by the present model. In order to do that, combination with Lagrangian model is essential.

REFERENCES

Abramovich, G.N., (1963), The Theory of Turbulent Jets, MIT Press, Cambridge, Massachusetts, USA

Anantharamaiah, N., Vahedi, H., Pourdeyhimi, B., (2006), A Study on Hydroentangling Waterjets and Their Impact Forces, Experiments in Fluids, v41, pp. 103–113

Arai, M., Shimizu, M., Hiroyasu, H., (1988), Breakup Length and Spray Formation Mechanism of a High Speed Liquid Jet, ICLASS-88, pp. 177–184

FUENT 6.3 USER MANUAL

Guha, A., Barron, R.M., Balachandar, R., (2007), Experimental Study and CFD Modeling of High Speed Water Jets in Air, 60th Annual Meeting of APS-DFD, Salt Lake City, Utah, USA

Guha, A., Barron, R.M., Balachandar, R., (2008), Numerical Simulation of High Speed Water Jets in Air, Accepted in the 16th Annual Conference of the CFD Society of Canada, CFD2008, Saskatoon, Saskatchewan, Canada

Hiroyasu, H., Arai, M., Shimizu, M., (1991), Break-up Length of a Liquid Jet and Internal Flow in a Nozzle, ICLASS – 91, pp. 275–282

Hiroyasu, H., (2000), Spray Breakup Mechanism from the Hole-Type Nozzle and its Applications, Atomization and Sprays, v10, pp. 511–521

Hoyt, J.W., Taylor, J.J., (1977), Waves on Water Jets, Journal of Fluid Mechanics, v83, pp. 119-127

Leu, M.C., Meng, P., Geskin, E.S., Tismeneskiy, L., (1998), Mathematical Modeling and Experimental Verification of Stationary Water Jet Cleaning Process, Journal of Manufacturing Science and Engineering, v120, pp. 571-579

Lin, S.P., Reitz, R.D., (1998), Drop and Spray Formation from a Liquid Jet, Annual Review of Fluid Mechanics, v 30, pp. 85–105

McCarthy, M.J., Molloy, N.A., (1974), Review of Stability of Liquid Jets and the Influence of Nozzle Design, Chemical Engineering Journal, v7, pp. 1–20

Rajaratnam, N., Steffler, P.M., Rizvi, S.A.H., Smy, P.R., (1994), Experimental Study of Very High Velocity Circular Water Jets in Air, Journal of Hydraulics Research, v32, n3, pp. 461-470

Rajaratnam, N., Albers, C., (1998), Water Distribution in Very High Velocity Water Jets in Air, Journal of Hydraulic Engineering, v124, n6, pp. 647-650

Rayleigh, W.S., (1878), On the Instability of Jets, Proceedings of the London Mathematical Society, v10, p. 4

Sallam, K.A., Faeth, G.M., (1999), Drop Formation at the Surface of Plane Turbulent Liquid Jets in Still Gases, International Journal of Multiphase Flow, v25, pp. 1161–1180

Sallam, K.A., Dai, Z., Faeth, G.M., (2002), Liquid Breakup at the Surface of Turbulent Round Liquid Jets in Still Gases, International Journal of Multiphase Flow, v28, pp. 427–449

Sou, A., Hosokawa, S., Tomiyama, A., (2007), Effects of Cavitation in a Nozzle on Liquid Jet Atomization, International Journal of Heat and Mass Transfer, v50, pp. 3575–3582

Sterling, A.M., Sleicher, C.A., (1975), The Instability of Capillary Jets, Journal of Fluid Mechanics, v 68, pp. 477–495

Tamaki, N., Shimizu, M., Hiroyasu, H., (2001), Enhancement of the Atomization of a Liquid Jet by Cavitation in a Nozzle Hole, Atomization and Sprays, v11, pp. 125–137

Vahedi Tafreshi, H., Pourdeyhimi, B., (2003), Effects of Nozzle Geometry on Waterjet Breakup at High Reynolds Numbers, Experiments in Fluids, v35, pp. 364–371

Weber, C., (1931), Zum Zerfall Eines Flussigkeitsstrahles. Zeitschrift Fur Angewandte Mathematik Und Mechanik, v11, pp. 138–145

Yanaida, K., Ohashi, A., (1978), Flow Characteristics of Water Jets in Air, In Proceedings of 4th International Symposium on Jet Cutting Technology, BHRA Fluid Engineering, Cranfield, UK, pp. 39-54

Yanaida, K., Ohashi, A., (1980), Flow Characteristics of Water Jets in Air, 5th International Symposium on Jet Cutting Technology, BHRA Fluids Engineering, Hanover, F.R. Germany, pp. 33-44

Yoon, S.S., Hewson, J.C., DesJardin, P.E., Glaze, D.J., Black, A.R., Skaggs, R.R., (2004), Numerical Modeling and Experimental Measurements of a High Speed Solid-Cone Water Spray for Use in Fire Suppression Applications, International Journal of Multiphase Flow, v30, pp. 1369–1388

Zou, C-S., Dang,L., Duan,X., Cheng,D.Z., (1985), Investigation on Anatomy of Continuous Waterjet for Updating Jet Performance, Proceedings of 3rd American Waterjet Conference, Pittsburg, U.S.A, pp. 160-178

APPENDIX

A.1 Uncertainty Analysis

This section contains the error estimation for the various measurements and results reported in this study. In the experiments, we used two pressure transducers, one at the nozzle inlet and the other at the target plate. We also used a Linear Variable Displacement Transducer (LVDT). Also, we used a scale to measure the Spread Coefficient of the jet.

A.1.1 Uncertainty Analysis of Pressure Transducer

Range	0-2000 psi
Input Voltage	0.468-10.397 V
Output Voltage	0-100 mV
Accuracy (e)	Combined Linearity,Hysterisis and Repeatability ± 0.25%
Resolution	Negligible
Bias (b)	± 2%

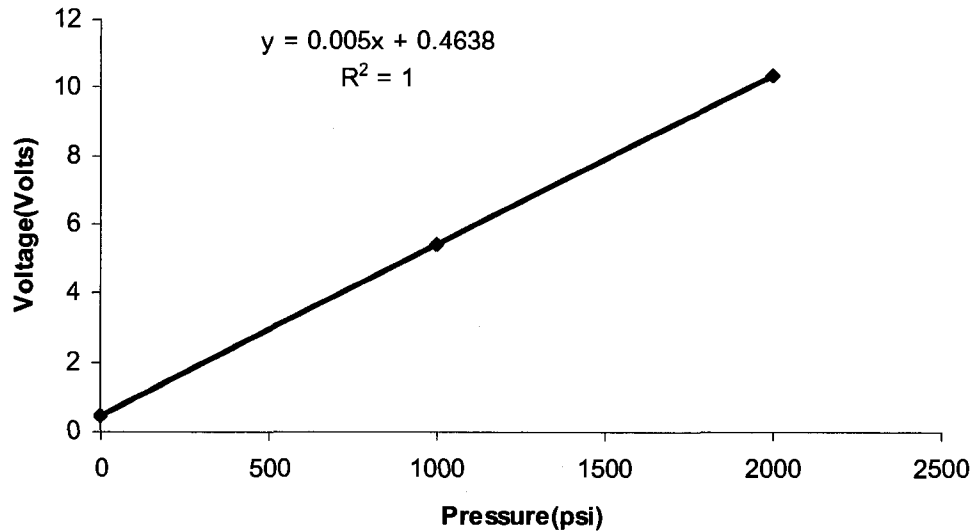**Table A.1.1: Specifications of the Pressure Transducers**

Figure A.1.1: Calibration Curve of the Pressure Transducer

The Sensitivity of the Pressure Transducers is obtained from the Calibration Curve. The obtained value is 0.005 V/psi.

Assumption: Values representative of the instrument at 95% probability.

Since resolution is negligible, hence Zero Order Uncertainty is negligible. Also, the output voltage from the pressure transducer is read by a Data Acquisition System whose uncertainty is negligible.

The Design Stage Uncertainty (U_d) is given by

$$U_d = b \pm \sqrt{e^2} \quad (95\%)$$

Or, $U_d = \pm 0.02 \pm 0.0025$ V (95%)

Or, $U_d = \pm 0.0001 \pm 0.0000125$ psi (95%)

A.1.2 Uncertainty Analysis of Linear Variable Displacement Transducer

Range	± 15 inches
Input Voltage	0-5 V
Output Voltage	24-40 V
Sensitivity	1.5 inches/V
Linearity Error (e_l)	± 0.5%
Bias (b)	Negligible
Resolution	Negligible

Table A.1.2: Specifications of the LVDT

Assumption: Values representative of the instrument at 95% probability.

Since resolution is negligible, hence Zero Order Uncertainty is negligible. Also, the output voltage from the pressure transducer is read by a Data Acquisition System whose uncertainty is negligible. The Design Stage Uncertainty (U_d) is given by

$$U_d = b \pm \sqrt{e_l^2} \quad (95\%)$$

Or, $U_d = \pm 0.005$ V   (95%)

Or, $U_d = \pm 0.0075$ inches (95%)

A.1.3 Uncertainty Analysis of the Scale

A scale of range 0-30 cm and resolution of 1 mm was used to measure the spread of the jet. The Zero Order Uncertainty (U_o) of the scale is

$$U_o = \pm 0.5 \times 1 = \pm 0.5 \text{ mm } (95\%)$$

A.1.4 Uncertainty in Measuring the Jet Width

The spread of the jet was measured with the help of the scale placed at 100 mm from nozzle exit. The Zero Order Uncertainty of the scale was ± 0.5 mm. The errors in measuring the width of the jet for different test cases are given in the table below.

Test Case	Jet Width (mm)	Spread Coefficient (C)	Error (%)
1	4.8	0.012	10.42
2	6.4	0.028	7.81
3	7.3	0.037	6.85
4	7.9	0.043	6.33
5	9.2	0.056	5.43

Table A.1.3: Error Estimation in Measuring the Jet Width

VITA AUCTORIS

Anirban Guha was born in 1980 in Kolkata, West Bengal, India. He graduated from Jadavpur University, Kolkata, India with a Bachelors degree in Mechanical Engineering in June 2004. He worked in Computational Thermo-fluids Laboratory of Jadavpur University as a Research Fellow for more than a year. Presently Mr. Guha is pursuing his Master of Applied Science degree in the Department of Mechanical, Automotive and Materials Engineering at the University of Windsor, Windsor, Ontario, Canada with specialization in Fluid Mechanics and expects to graduate in April 2008.